DETERMINING CO_2-BRINE RELATIVE PERMEABILITY FOR CO_2 SEQUESTRATION: A PORE NETWORK MODELLING STUDY

A THESIS SUBMITTED TO
THE BOARD OF GRADUATE PROGRAMS
OF
MIDDLE EAST TECHNICAL UNIVERSITY, NORTHERN CYPRUS CAMPUS

BY

THRAIYE SEIF HEMED

IN PARTIAL FULFILLMENT OF THE REQUIREMENTS
FOR
THE DEGREE OF MASTER OF SCIENCE
IN SUSTAINABLE ENVIRONMENT AND ENERGY SYSTEMS PROGRAM

AUGUST 2023

Approval of the Board of Graduate Programs

Prof. Dr. Cumali Sabah

Chairperson

I certify that this thesis satisfies all the requirements as a thesis for the degree of Master of Science

Asst. Prof. Dr. Canraş Batunlu

Program Coordinator

This is to certify that we have read this thesis and that in our opinion it is fully adequate, in scope and quality, as a thesis for the degree of Master of Science.

Asst. Prof. Dr. Doruk Alp

Supervisor

Examining Committee Members

Prof. Dr. Salih Saner	NEU/PNGE	
Prof. Dr. Murat Fahrioğlu	METU NCC/EEE	
Asst. Prof. Dr. Doruk Alp	METU NCC/PNGE	

I hereby declare that all information in this document has been obtained and presented in accordance with academic rules and ethical conduct. I also declare that, as required by these rules and conduct, I have fully cited and referenced all material and results that are not original to this work.

Name, Last name : Thraiye, Seif Hemed

Signature :

ABSTRACT

DETERMINING CO_2-BRINE RELATIVE PERMEABILITY FOR CO_2 SEQUESTRATION: A PORE NETWORK MODELLING STUDY

Seif Hemed, Thraiye
Master of Science, Sustainable Environment and Energy Systems Program
Supervisor: Asst. Prof. Dr. Doruk Alp

August 2023, 102 pages

Predicting CO_2 migration in the subsurface after its injection is crucial for successful long-term fluid storage. Relative permeability is one of the essential parameters that aid in accurately predicting injectivity, plume migration, and residual CO_2 trapping. Despite the existing literature on CO_2-brine relative permeability, there still needs to be more data to understand the behaviour of CO_2 after being injected into the subsurface for future predictions. However, lab-based relative permeability experiments are usually expensive and time-consuming. This research focuses on conducting pore network modelling experiments using OpenPNM, an open-source Python package. It compares the results with lab-based experimental and other PNM-generated results to verify OpenPNM's reliability as a cheaper, faster and easily accessible solution. Regardless of the lithology, homogeneous samples (Berea sandstone and a carbonate) exhibited a good match of results. However, a relatively heterogeneous sample (Mt Simon sandstone) did not have matching relative permeability curves. When altering the network parameters in OpenPNM, spacing impacted absolute permeability but had no effect on relative permeability, a larger shape value generated smoother curves but required higher computational power, and a larger connectivity value caused a shift of the relative permeability curves to the right.

Keywords: CO_2-brine Relative Permeability, Pore Network Modelling (PNM), CO_2 Sequestration.

ÖZ

CO_2 YERALTI DEPOLAMASI İÇİN CO_2-SU GÖRELİ GEÇİRGENLİĞİ BELİRLEME: BİR GÖZENEK AĞI MODELİ ÇALIŞMASI

Seif Hemed, Thraiye
Yüksek Lisans, Sürdürülebilir Cevre ve Enerji Sistemleri
Tez Yöneticisi: Yrd. Doç Dr. Doruk Alp

Ağustos 2023, 102 sayfa

Enjeksiyon sonrası yeraltında CO2 taşınımını tahmin etmek, uzun vadede başarılı depolama için çok önemlidir. Göreli geçirgenlik, enjektivite, akışkan taşınımı ve CO2 hapsinin doğru tahmin edilmesinde temel parametrelerden biridir. CO2-su göreli geçirgenliği üzerine mevcut literatüre rağmen, CO2'nin yeraltına enjekte edildikten sonra davranışını anlamak için hala daha fazla veriye ihtiyaç vardır. Ancak, laboratuvarda yapılan göreli geçirgenlik deneyleri maliyetli ve zahmetlidir. Bu araştırmada, açık kaynaklı bir Python paketi olan OpenPNM kullanarak gözenek ağı modeli çalışmaları yapılmıştır. Model sonuçları, daha ucuz, daha hızlı ve kolay erişilebilir bir çözüm olarak açık kaynak paketin güvenilirliğini doğrulamak için laboratuvar deneyleri ve diğer gözenek ağı modelleri karşılaştırılmıştır. Litolojiden bağımsız, homojen numune (Berea kumtaşı ve bir karbonat) sonuçları iyi bir uyum sergilemiştir. Bununla birlikte, nispeten heterojen bir örnek (Mt Simon kumtaşı) göreli geçirgenlik eğrileri uyuşmamıştır. OpenPNM'de ağ parametrelerini değiştirirken, gözenekler arasındaki mesafenin mutlak geçirgenliği etkilediği, ancak göreli geçirgenlik üzerinde hiçbir etkisi olmadığı, artan geometric katsayının daha yumuşak eğriler oluşturduğu ancak daha yüksek hesaplama gücü gerektirdiği ve

artan bağlantı değerinin göreli geçirgenlik eğrilerinin sağa kaymasına neden olduğu gözlemlenmiştir.

Anahtar Kelimeler: CO_2-su Göreli Geçirgenlik, Gözenek Ağı Modeli, CO_2 Depolama/saklama.

To a Carbon-Free Sustainable Future

ACKNOWLEDGMENTS

I would like to express my sincere gratitude and appreciation to all those who have supported and contributed to the completion of this thesis. Their encouragement, guidance, and assistance have been invaluable, and I am deeply indebted to them.

First and foremost, I extend my heartfelt thanks to my thesis supervisor, Asst. Prof. Dr. Doruk Alp, for his unwavering support, patience, and insightful feedback throughout this research. His mentorship and has been instrumental in shaping this work.

I am also grateful to the external support and guidance offered by Mr. Uğur Paköz from Turkish Petroleum. His knowledge on core analysis was critical in steering us towards a practical experimental setup and connections. I would also like to thank the Premier Corex team for their valuable expertise on the subject through whom we learnt a lot about the new hybrid technique.

I am deeply appreciative of my family for their unconditional love and understanding. Their belief in my abilities has been a driving force behind my perseverance. Additionally, I would like to acknowledge the valuable insights, encouragement and support from my friends particularly Syed Sameer Noman and Chiedozie Augustine Ike-Offiah.

To everyone who has played a part, big or small, in this academic endeavor, I offer my heartfelt appreciation. Your support has been pivotal in shaping the culmination of this thesis.

Thank you all.

TABLE OF CONTENTS

LIST OF TABLES

TABLES

LIST OF FIGURES

FIGURES

LIST OF ABBREVIATIONS

ABBREVIATIONS	
BT	Breakthrough
CCS	Carbon Capture and Storage
CEE	Capillary End Effects
DNS	Direct Numerical Simulation
EOR	Enhanced Oil Recovery
LBM	Lattice Boltzmann Method
LNG	Liquified Natural Gas
MB	Maximal Ball
MIP	Mercury Intrusion Porosimetry
NMR	Nuclear Magnetic Resonance
PNM	Pore Network Modelling
sc	Supercritical
SEM	Scanning Electron Microscope

LIST OF SYMBOLS

SYMBOLS

K	Hydraulic Conductivity
k	Permeability
k_r	Relative Permeability
k_{rco2}	CO_2 Relative Permeability
P_c	Capillary Pressure
S_g	Gas Saturation
S_{or}	Residual Oil Saturation
S_{rg}	Residual Gas Saturation
S_w	Water Saturation
S_{wc}	Connate Water Saturation
S_{wi}	Irreducible Water Saturation

CHAPTER 1

INTRODUCTION

In the era that we live in, it is not peculiar to come across infamous headlines like “Heatwave across Europe causes the highest temperatures to have ever been recorded in the area (European Environment Information and Observation Network , 2022)”, “Pakistan gets drowned in floods caused by the monsoon rains affecting around 33 million people (UNICEF, 2022)” or “Australia gets hit by wildfires impacting around 3 billion animals and 19 million hectares of burnt land (WWF Australia, 2020)”. What they all have in common, despite their differences, is that they are all climate change-related catastrophes. Climate change refers to a long-term shift in temperatures and weather patterns due to natural or man-made factors (Alley, et al., 2007). The signs of climate change are all around us: melting glaciers, changing seasons, and extreme weather conditions like drought, floods and hurricanes. Since the industrial revolution in the late 1800s, man-made activities have led to increased emissions that accelerated climate change, causing the loss and degradation of ecosystems, increased mortality rates, lowered life standards, reduced water and food security, increased damage to infrastructure, and displacement and migration of humans (Begum, et al., 2022). This has led to labelling climate change as a matter of high urgency that demands globally coordinated solutions.

To address the crisis, several scientists and organisations have come up with ways of understanding the earth's systems and plausible solutions. In 2009, Johan Rockström, who led a group of 28 other scientists, came up with the 9-planetary boundaries within which humanity can continue to develop and thrive. These boundaries are stratospheric ozone depletion, loss of biosphere integrity (biodiversity loss and extinctions), chemical pollution and the release of novel entities, climate change, ocean acidification, freshwater consumption and the global

hydrological cycle, land system change, nitrogen and phosphorus flow to the biosphere and oceans, and atmospheric aerosol loading.

As far as climate change goes, it is stated that it is imperative for the greenhouse gas emissions to be halted and decreased from the atmosphere in order to bend the curve. Global agreements like the Paris Agreement guide all nations to reduce greenhouse gas emissions to stop global warming. The initial goal is not to allow the global temperature to increase by more than 2˚C while aiming for a future limit of 1.5˚C (United Nations, 2016). To achieve its goals, the treaty incorporates several key elements, including but not limited to mitigation, transparency, adaptation and support (United Nations, 2017). Climate mitigation solutions include improving energy efficiency, switching to less carbon-intensive fuels, enhancing biological sinks, and reducing non-CO_2 greenhouse gas emissions and CO_2 capture and storage (IPCC, 2005). CO_2 capture and storage are the subject of interest in this research, focusing on storage.

1.1 Background on CCS

Carbon dioxide capture and storage (CCS) is a process of separating CO_2 from industrial and energy-related sources, transport to a storage location and long-term isolation from the atmosphere (IPCC, 2005). There are several ways of isolating CO_2 from the atmosphere, including geological storage (which will be discussed in detail), ocean storage and mineral carbonation. Geological storage of CO_2 involves injecting the fluid into depleted oil and gas reservoirs, saline aquifers or as part of enhanced oil and gas recovery.

Once CO_2 is injected into a reservoir, several processes account for the fluid's storage. Considering a saline aquifer as the storage medium described here, the reservoir is typically occupied by formation water, also known as brine. Above the reservoir is an impermeable layer (which does not allow fluid to flow through) called a cap rock that acts as a seal to trap fluid underneath. Figure 1.1 shows the migration

of CO_2 injected at the rim of an anticline. In the saline aquifer, CO_2 starts migrating upwards due to its lower density until it reaches a cap rock that blocks it from rising upwards. This process is called **structural trapping** (Burnside & Naylor, 2014). While migrating upwards, some CO_2 remains trapped in the rock along with the formation water, a process called **residual trapping**. Some CO_2 dissolves in the brine, forming an acidic solution which reacts with the rock-forming minerals on the rock surface. This process is called **dissolution and mineral trapping** (Zhang & Song, 2014). Additionally, some CO_2 will stick to a rock's clay minerals undergoing **adsorption** (Golding, et al., 2011), another storage mechanism commonly found in coal systems. Furthermore, an aquifer, flowing under the anticline surrounding the trapped CO_2, will block the CO_2 from escaping laterally, also known as the "spill point" of CO_2. This mechanism is called **hydrodynamic trapping** (Rosenbauer & Thomas, 2010). Figure 1.1 is a cross-sectional view of a saline aquifer illustrating structural, residual, dissolution, and mineral trapping. The expanded views of the mechanisms are shown on the right.

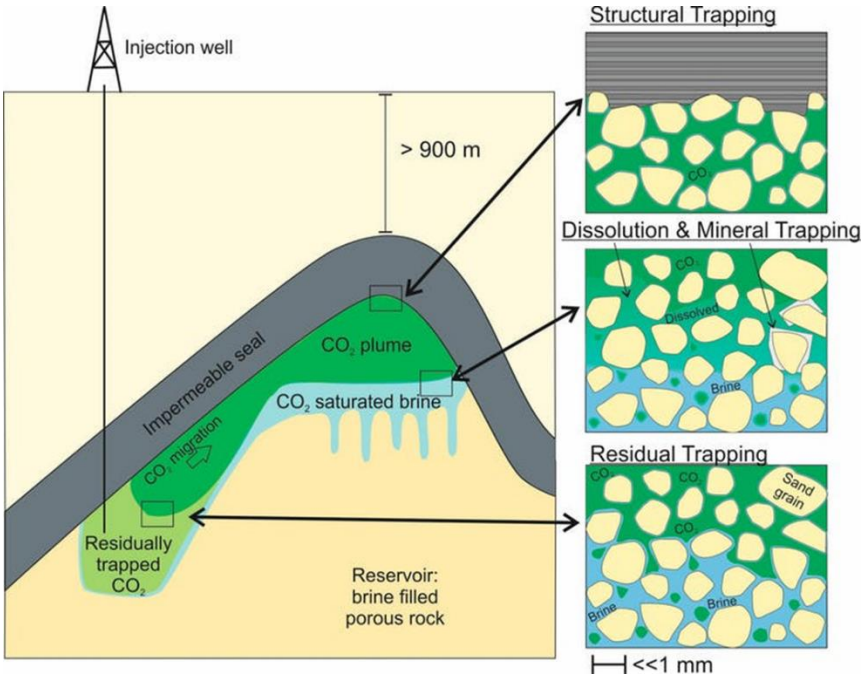

Figure 1.1 Illustration of CO_2 storage mechanisms in a saline aquifer (Flude, 2020).

1.2 Sustainability Aspect of CCS

Studies show that CCS has the potential to store up to 1,000-10,000 Gt in saline aquifers and 920 Gt in depleted oil and gas fields (Yang et al., 2010). The capacity is estimated to increase as unconventional resources such as coal bed methane and gas hydrate potential are yet to be evaluated. CCS technology can aid in lowering the emissions from power plants and industries, accounting for more than 30% of total emissions (Ritchie et al., 2020).

To understand the potential of CCS, it is better to consider its capacity relative to tree sequestration capacity. For an estimate of matured oak trees storing 29 kg of CO_2/tree for one year (Cannell, 1999), 35 trillion trees will be required to sequester 1,000 Gt of CO_2 per year. This will require around 138 billion hectares of woodland forests, assuming moderate density where 250 trees occupy 1 hectare of land, whilst the whole world has a total land area of 13 billion hectares. If the whole world's land is to be covered in trees, it will take approximately 11 years to sequester 1000 Gt of CO_2.

During the CCS process, emissions are produced in power plants or other industries during the capture stage. These emissions are from the energy required to capture the CO_2. Based on the source of energy used, the estimated emissions will vary. Another stage of emissions is during transportation, mainly when using ships and during compressions of CO_2. The final stage of emissions is during the storage process, where energy is required to inject CO_2 underground. However, although there are no actual figures, the total CO_2 emissions throughout the CCS process are estimated to be insignificant compared to the amount stored.

Some of the exemplary CCS mega projects worldwide already being executed include the Northern Lights in Norway, the Alberta Carbon Trunk Line in Canada, and the Gorgon CO_2 injection project in Australia.

1.3 Problem Statement

In CO_2 storage, once injected into the subsurface formations, the CO_2 is bound to flow in different directions in a geological timescale. During the migration of CO_2 in the reservoir, it may come across fractures that may allow leakage into the atmosphere. To ensure successful long-term storage, it becomes essential to understand how CO_2 will flow against brine in a rock. Relative Permeability is an important parameter that describes how easily a fluid flows against another in a porous medium.

Relative permeability data is essential for accurately predicting injectivity, plume migration, and residual CO_2 trapping. Relative Permeability is a rock property as much as it is a fluid property. Thus, it shows variations according to rock and fluid types. Considering geological heterogeneity, relative permeability may vary significantly from point to point, even for the same rock type or within the same formation. Therefore, there exists a natural uncertainty in the relative permeability.

To predict CO_2-brine relative permeability, core-flooding experiments can be conducted in the laboratory on desired core samples. However, this method is tedious and expensive, making it not a feasible solution for many. Instead of conducting laboratory-based experiments, computer simulations are an affordable and faster solution. In this study, CO_2-brine relative permeability is predicted using computer-based experiments utilising pore-scale modelling approach.

1.4 Overview of the Thesis Structure

This thesis starts with a literature review after the introduction section, where the CO_2 phase change, a crucial aspect of the CCS process, is looked upon. Then, the background on relative permeability and its significance in CCS studies are explained. The following sections describe the different approaches to conducting relative permeability experiments, from lab-based experiments to computer simulations. The Pore Network Modelling approach, the chosen method in this

research, is assessed in detail before showing previous studies on the subject and comparing existing results in the literature.

The next chapter on methodology describes the chosen tool for this study and the data required to run the simulation. This chapter will tabulate the rock and fluid properties of different samples obtained from the literature used in the study. Finally, the results are discussed by comparing them to previous results in the literature and evaluating factors affecting relative permeability curves before concluding.

CHAPTER 2

LITERATURE REVIEW

2.1 CO_2 Phase Change During CCS

One of the important characteristics of CO_2 to understand during CCS is its phase change. CO_2 exists in the gaseous phase at atmospheric conditions and lower temperatures and pressures. At higher pressures but lower temperatures, the phase is solid. During transportation, CO_2 is compressed so that it may convert to liquid. The liquid phase is usually the preferred fluid state during transportation, as is the case for LNG, since it takes up less volume, making it easier to handle. Figure 2.1 shows that the typical ship storage conditions of CO_2 are within the saturation line where the fluid is in liquid form, and the pipeline conditions are at higher temperatures also in the liquid phase. Above the critical point where the temperature and pressure are much higher, CO_2 is in the supercritical phase. In the supercritical phase, distinct liquid and gas phases do not exist. This is the phase of the fluid when stored in reservoirs where the conditions are high temperature and pressure.

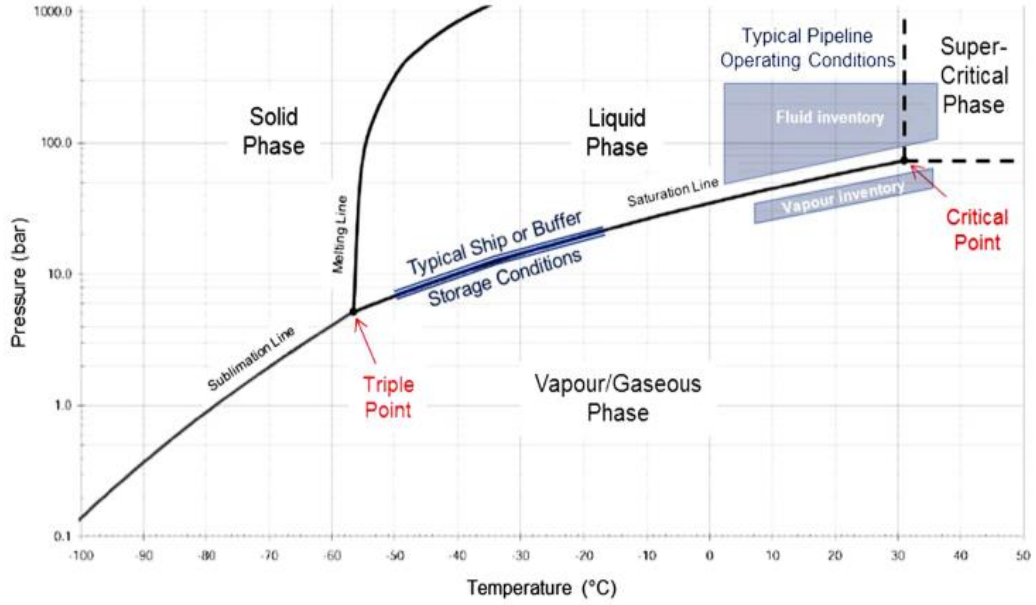

Figure 2.1 CO_2 phase diagram showing the different fluid states during transportation (Holt et al., 2012).

2.2 Absolute Permeability

When a fluid is injected into a porous medium, it will flow through the pore spaces (voids) of the medium. The easiness of how that fluid will move in the pore space is referred to as **absolute permeability**. It is an empirical constant of Darcy's equation, a fundamental single-phase fluid flow relationship. Equation (2.1) is Darcy's equation where q is the total flow rate, k is the permeability, A is the cross-sectional area of the flow medium, μ is the fluid viscosity, Δp is the change in pressure across the flow medium, and L is the length of the flow medium (Darcy, 1856). Figure 2.2 demonstrates the mentioned parameters on a cylindrical porous medium. Estimating absolute permeability using Darcy's equation requires knowing the fluid flow rate, pressure drop, and fluid properties.

$$q = \frac{kA}{\mu}\frac{\Delta p}{L} \tag{2.1}$$

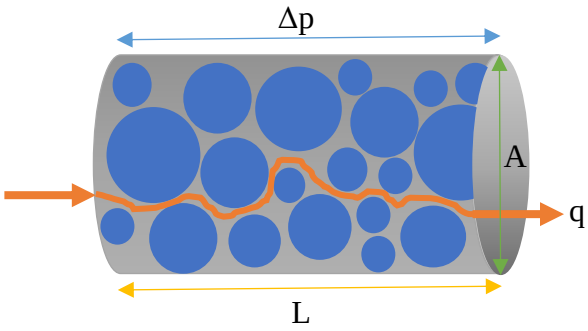

Figure 2.2 A demonstration of fluid flowing in a porous medium highlighting the Darcy's equation parameters.

However, experimentally derived relationships can be used to obtain absolute permeability for cases where the fluid flow properties are not given. Kozeny-Carman is a theoretical equation based on the capillary bundle that uses the geometrical properties of the flowing medium to obtain its absolute permeability, as shown in Equation (2.2) (Carman, 1937). In this equation, k is absolute permeability, Ψ is sphericity, Φ is porosity, and d_g is the average diameter of sand grains. Figure 2.3 shows the Kozeny-Carman relationship between porosity and absolute permeability. It can be seen that there is a directly proportional relationship between the two parameters.

$$k = \psi_s^2 \frac{\phi^3 d_g^2}{180(1-\phi)^2} \tag{2.2}$$

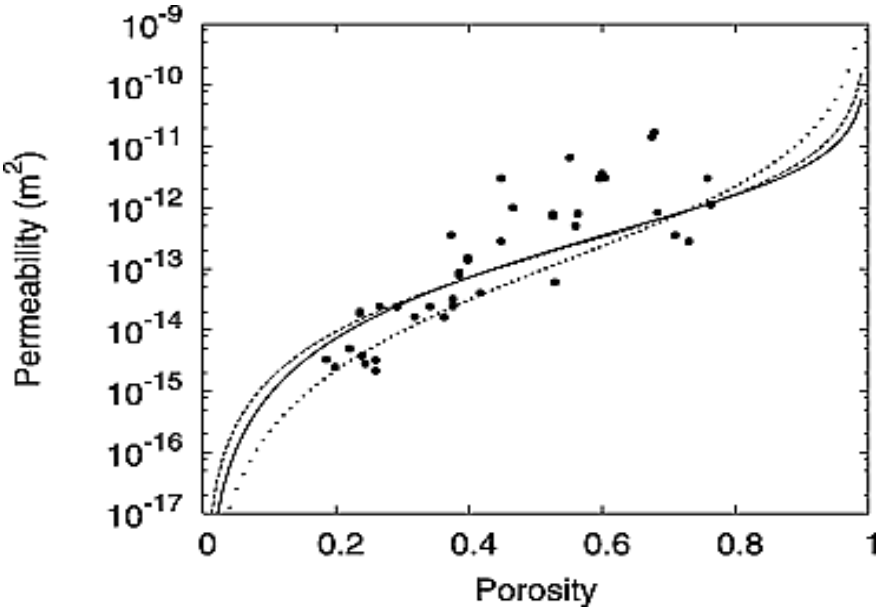

Figure 2.3 Porosity and permeability relationship for a porous media estimated using the Kozeny-Carman relationship (Costa, 2006).

2.3 Relative Permeability and its Importance in CCS

In typical reservoir conditions, there exist either two or three fluid phases. When the easiness of a fluid flowing against the other fluid(s) in the pore space is to be determined, the concept of **relative permeability** is introduced. **Relative permeability** is the ratio of effective to base permeability, as shown in Equation (2.3). The value of relative permeability ranges from 0 to 1 as it results from normalizing one permeability value to another (effective to absolute). **Effective permeability** is the ability of a fluid to flow in the presence of another fluid in the medium. **Absolute permeability** is a property that determines how easily a fluid flows through a porous medium. When two fluids are flowing in a medium, the absolute permeability is usually chosen as the one measured at the beginning of the experiment at irreducible saturation.

$$k_r = \frac{k_e \ @S_{w2}}{k \ @S_{w1}} \tag{2.3}$$

Relative permeability is dependent on fluid saturation. Therefore, the relationship between the two parameters generates relative permeability curves used for analysis. Commonly, steady-state, or unsteady-state core-flood experiments are conducted to obtain relative permeability relationships. Figure 2.4 (a) shows how the fluid saturations change during an unsteady state coreflooding experiment. It starts with a 100% brine-saturated core, which is drained with oil until irreducible water saturation is reached. At first, water permeability could be measured, and then oil relative permeability at irreducible water saturation is measured. The next stages involve the imbibition process, where the oil in the core is displaced by the injected brine and saturation keeps changing until the water breakthrough[1] is reached and, eventually, the residual oil saturation in the end. The relative permeability curves in Figure 2.4 (b) represent the unsteady state process. When the core only allows the flow of oil at irreducible water saturation, point A stands for the oil's relative permeability and point B for water. Since water is immobile at irreducible saturation, water's relative permeability at that point is 0 and oil, being the only mobile phase, has a relative permeability of 1 with respect to effective oil permeability at S_{wir}. As water is flooded into the core, the relative permeability of water keeps increasing while that of oil keeps decreasing till it reaches residual oil saturation, where it is 0.

[1] Breakthrough is a term used to describe the situation where an injected fluid starts flowing out from the opposite end.

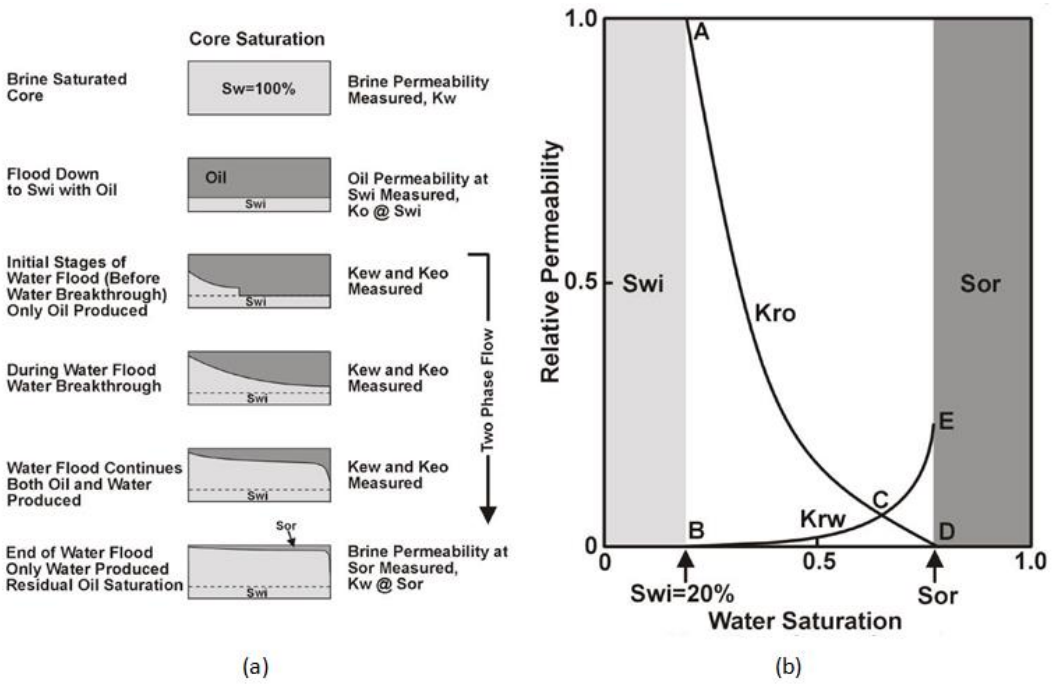

Figure 2.4 a) Unsteady state waterflooding procedure b) Generated relative permeability curve for the unsteady state waterflooding experiment (Kantzas et al.).

In underground carbon storage, relative permeability is one of the important factors in determining fluid transport. Relative permeability relationships can be used to predict CO_2 plume migration, approximate the range of injectivity and estimate the optimum number of injection wells. Several studies have shown that the relative permeability curves' characteristics can be used to derive the distribution of CO_2 in the porous media (Doughty & Pruess, 2004; Flett et al., 2004 and Koop et al., 2009). In a study by Moodie et al. (2017), it is mentioned that the relative permeability relationship controls the saturation of each phase (CO_2 and brine) present, hence controlling the supercritical plume migration and phase behaviour.

Additionally, Burton et al. (2009) proved the significance of relative permeability for CO_2 injectivity into brine aquifers. In their paper, they showed how the injection flow rate changed as the Brooks-Corey fitting parameters were altered. The flow rate varied by almost 20% when the parameters were changed. Wegener & Harpole (1996) also conducted research that concluded a decreased CO_2 injection rate when

the measured CO_2 relative permeability (k_{rCO2}) is lowered, which is shown in Figure 2.5. The dependency of flow rate to the relative permeability curves enables the estimation of the optimum number of injection wells to achieve the desired overall injection rate (Burton et al., 2009).

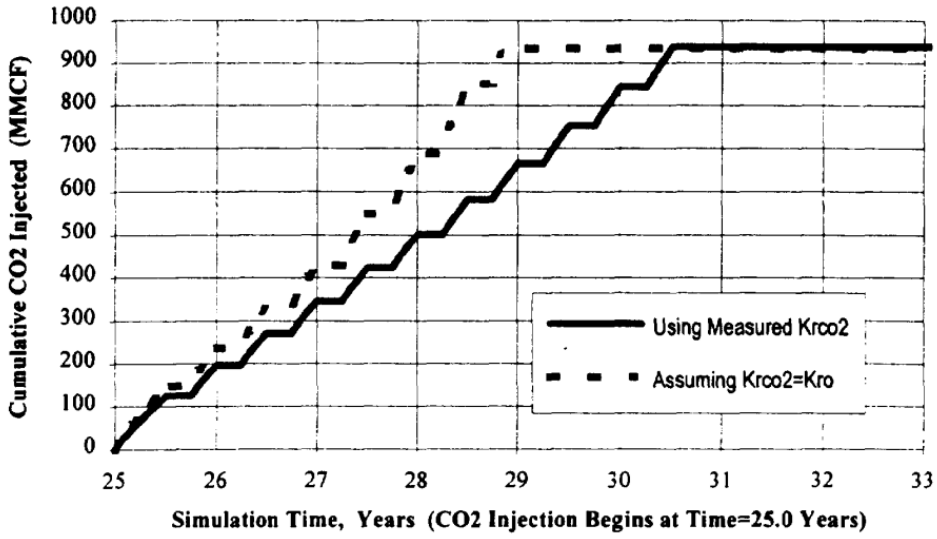

Figure 2.5 Lowered CO_2 injection rate when the measured $krCO_2$ is lower (Wegener & Harpole, 1996).

The implication of the relative permeability of CO_2-brine systems is also shown in another experimental study by Burnside & Naylor (2014) on residual trapping of CO_2. In the pore spaces where both CO_2 and brine exist, CO_2, being less dense, will migrate upwards. However, some residual CO_2 will remain trapped in the pore spaces filled with brine. At this point, the $krCO_2$ reads as 0 on the relative permeability relationship.

Nevertheless, Akbarabadi & Piri (2013) have shown that the relative permeability of brine increases dramatically when trapped CO_2 dissolves in the solution, demonstrating another dependence of the curves. In their research, excess brine was injected into cores containing residual CO_2. In the beginning, the brine had lower relative permeability values due to CO_2 blockage. As CO_2 dissolves, more brine is

allowed to flow freely without blockage, hence the increase in its relative permeability. Figure 2.6 a) and b) shows the increase in brine relative permeability with dissolution of CO_2 for Berea and Nugget sandstone samples.

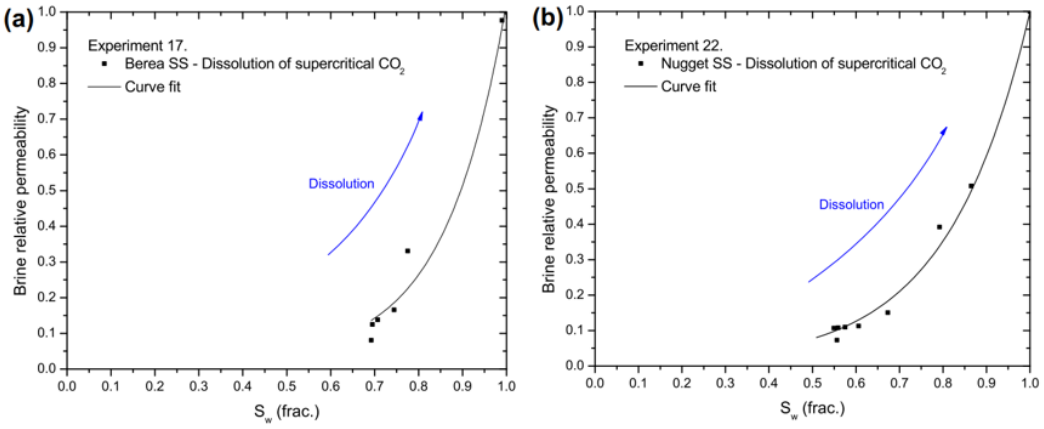

Figure 2.6 Increase in brine relative permeability with the dissolution of CO_2 for a) Berea SS and b) Nugget SS (Akbarabadi & Piri, 2013).

For a long time, there has been a gap in the literature for CO_2-brine relative permeability, mostly derived from mathematical equations or recent experimental data that have exhibited uncertainty in the data range. To successfully predict significant effects like plume migration, conducting more relative permeability experiments is of crucial importance. The most reliable methods are laboratory-based experimental ones, which include different methods that will be discussed in detail in the next section. Though reliable, the lab-based experimental methods for conducting relative permeability experiments are expensive and tedious. The other methods are numerical simulation-based, which are more affordable and easily accessible.

2.4 Review of Experimental Methods for Measuring Relative Permeability

To obtain relative permeability values at different fluid saturations, coreflooding experiments are usually conducted at a steady or unsteady state. For unsteady state experiments, first, the end-point effective permeability of one phase is measured against the other. Then, production data is recorded once the breakthrough point has reached to obtain a portion of the relative permeability curve. The breakthrough happens when the injected phase (that was at a residual saturation and injected at a constant flow rate or pressure) is produced at the outlet. Figure 2.3 from the previous section explains the unsteady state process in a simple diagram. Steady-state, on the other hand, involves injecting a series of fixed ratios of fluids until equilibrium is reached. For each ratio, after the equilibrium is reached, the produced fluids are separated, and rates are measured before reinjecting at different ratios.

There are several standard protocols developed to guide researchers on how to conduct these experiments, such as the book by McPhee et al. (2015) and the paper by Busch & Müller (2011). Figure 2.7 is a schematic representation of a relative permeability experimental setup for oil and water. Generally, relative permeability experiment setups consist of the following equipment:

a) Tanks/reservoirs containing fluids to be injected.
b) Pumps to control fluid flowrate and/or pressure entering the core.
c) Hassler-type core holder where the core sample is kept tightly.
d) Confining pressure pump for pressurising the sleeve surrounding the core.
e) Differential pressure gauges for measuring pressure difference between different points.
f) An oven/water bath to regulate the temperature at which the experiment is conducted.
g) Back pressure regulator to prevent backflow of fluid after exiting the core.
h) A device to measure fluid saturation. This could be done traditionally by volumetric method or advanced techniques like electric resistance or X-ray CT scans.

i) Effluent tank/reservoir to collect the output.

Between the two methods, the steady state method has a more complex experimental setup since it requires the simultaneous injection of two fluids. In contrast, an unsteady state involves the injection of a single phase at a constant rate or pressure. Additionally, steady-state experiments take longer duration to run compared to unsteady state experiments. While the former may typically last around 2-3 weeks, the latter may take only a day. Therefore, unsteady state experiments may prove to be more economical and time efficient. However, when it comes to the analysis of the collected data, the steady state experiment simply uses Darcy's equation, while the unsteady state experiment is more complex to analyse, requiring the use of fractional flow concepts like Buckley Leverett.

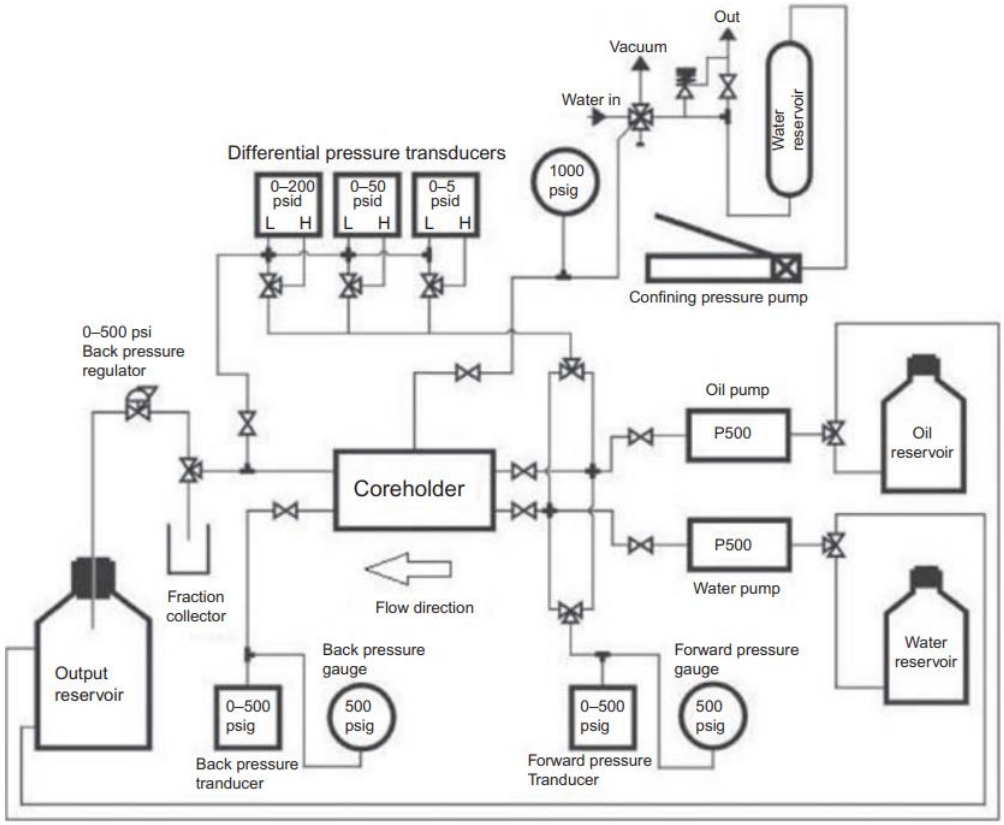

Figure 2.7 General relative permeability experiments setup schematic (McPhee et al., 2015).

2.4.1 The Intercept Method

To compensate for the tediousness of the traditional steady and unsteady state method, a new modified method was recently proposed-**the intercept method**. This method requires running a steady-state relative permeability test with several different flow rates for each saturation point on the fractional flow curve. Obtaining multiple (three or four) sets of rates (q), pressure drops (Δp), and saturation data allows for the assessment of capillary end effects (CEE) artefacts. Therefore, in this method, both phases are injected at different ratios and flow rates.

Commonly, high flow rate or high-pressure drop experiments are recommended to reduce capillary end effects. However, high flow rates may cause gas to strip light ends from oil (in gas/oil steady-state experiments) or cause fines-migration issues in a clay-rich rock. On the other hand, high-pressure drops can introduce strong gas compressibility effects. Hence, the intercept method is a less complex solution where the steady state relative permeability data collected from low flow rate and low-pressure drop conditions can be corrected (Gupta & Maloney, 2016).

To define the intercept in mathematical form, first, the Darcy equation for the water phase for a steady state coreflood experiment is shown in Equation (2.4). In this equation, the term $k_{rw}(S_w)k$ is the effective water permeability at the oil fractional flow, F_o. The rest of the terms are as defined in Equation (2.1). Due to capillary end effects during a test, the measured pressure drop will be more than the theoretical one. The theoretical pressure drop will basically be the difference between the measured pressure drop and the pressure drop due to capillary end effects, as represented by Equation (2.5). This is because CEE increases the measured pressure drop due to increased flow resistance at the entrance and exit of the core. When Equation (2.5) is rearranged, Equation (2.6) is obtained. Equation (2.6) is linear with $\Delta p_{w,CEE}$ as the intercept of the plot of $\Delta p_{w,Measured}$ against $q_{t,}$ shown in Figure 2.8 (a).

$$q_t(1-F_o) = \frac{k_{rw}(S_w)kA}{\mu_w L}\left(\Delta p_{w,Theoretical\ without\ CEE}\right) \tag{2.4}$$

$$q_t(1-F_o) = \frac{k_{rw}(S_w)kA}{\mu_w L}\left(\Delta p_{w,Measured} - \Delta p_{w,CEE}\right) \tag{2.5}$$

$$\Delta p_{w,Measured} = \left\{\frac{\mu_w L(1-F_o)}{k_{rw}(S_w)kA}\right\} q_t + \Delta p_{w,CEE} \tag{2.6}$$

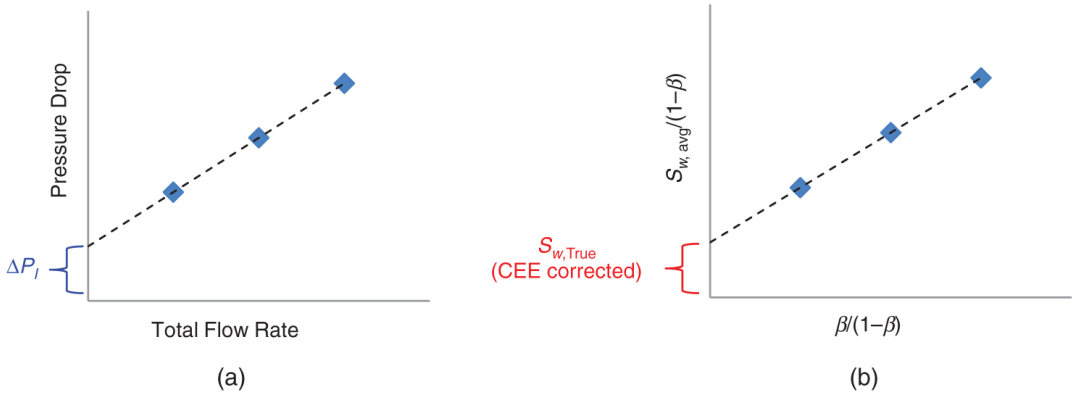

Figure 2.8 Plots used in the intercept method: a) The $\Delta P_{w,Measured}$ vs q_t plot with the pressure drop correction factor as the intercept, and b) the saturation plot for obtaining the saturation correction factor (Gupta & Maloney, 2016).

From the relationships explained above, the corrected pressure drop will be the difference between the measured pressure drop and the intercept (Δp_I) displayed in Equation (2.7). Hence, the plot of the corrected pressure drop against the total flow rate will yield a plot with a zero intercept. Upon obtaining the corrected pressure drop, the saturation can also be corrected using β, which is the CEE-length factor. The β value can mathematically be calculated using Equation (2.8). The saturation correction factor can then be obtained as the intercept of the plot of $S_{w,avg}/(1-\beta)$ against $\beta/(1-\beta)$ shown in Figure 2.8 (b).

$$\Delta p_{Corrected} = \Delta p_{Measured} - \Delta p_I \tag{2.7}$$

$$\beta = \frac{\Delta p_I}{\Delta p_{w,Measured} - \Delta p_I} \tag{2.8}$$

2.5 Pore Network Modelling as an Alternative Approach

When studying fluid flow in porous media, the continuum model, also known as the macroscopic model, is commonly used (Rapp, 2017). This model assumes that the porous media is a volume-averaged continuum, where macroscopic rock properties such as permeability, porosity and tortuosity describe the overall behaviour. Darcy's Law, Conservation of Mass, Conservation of Momentum and Conservation of Energy are among the mathematical equations utilised by the continuum model to describe fluid flow in porous media (Jacob & Yehuda, 1990). However, the volume-averaged approximation method may have limitations. It requires experimental data that may be challenging to measure, fails to account for microscopic features and is unable to predict phase distribution within the continuum (Miller, et al., 1998). Additionally, it cannot be applied in thin layers since the assumption of uniform properties within a control volume is not representative of such layers.

According to Blunt et al. (2013), apart from the continuum models, numerical simulation approaches like direct modelling and pore network modelling (PNM) are alternatives to describe fluid flow and transport in a porous media. The **direct modelling method** is also referred to as the lattice Boltzmann method (LBM), which is commonly used in the modelling of single and multiphase flow at pore scale models of porous media from images (Ramstad et al., 2019). This method involves discretising the voids (pore space) from a 3D image on a Cartesian grid, simulating the motion and collision of particles for the flow and transport computation (Blunt,

et al., 2013). The particles referred to herein are computational fluid elements (Lagrangian approach) used to simulate the fluid behaviour and do not represent physical particles like atoms or molecules. However, unlike PNM, the simulation of individual particles demands high computational power.

Pore network modelling (PNM) is an alternative method for simulating fluid flow in porous media that represents the geometry of the rock and the dynamics of the multiphase flow (Gostick, et al., 2016). Fatt (1956) was the first scientist to use a network of tubes as a representation of real porous media (Fatt, 1956). PNM addresses the limitations of continuum models mentioned in the first paragraph of this section i.e., the requirement of experimental data that may be challenging to measure, failure to account for microscopic features and inability to predict phase distribution within the continuum. The PNM method has been around for more than 40 years but started to be used for commercial purposes around 20 years ago. Reservoir engineers initially developed PNM to study oil flow in geological formations. Since it works on porous media, apart from Petroleum Engineering, it can be applied in different disciplines, including Chemical (Mohammadi et al., 2022), Soil Sciences (Mufti & Das, 2023), Biomedical (Guo, et al., 2010), Construction (Martins & Gonzalez, 2022), and Agriculture (Leitner et al., 2013).

Traditionally, heterogeneous porous media were thought to have random patterns, making reconstruction and modelling challenging. However, further studies, as discussed by Sahimi (2011), show how heterogeneities of a porous media or a fractured rock are not as random as once explained. In fact, they exhibit correlations at all length scales, hence introducing fractal distributions. Fractal distributions indicate the dependence of the length scale of the observations to property values in the region (Sahimi, 2011). Therefore, enabling the deduction of correlations to model porous media, hence laying a foundation for **pore network modelling**. PNM can give a more realistic description of fluid flow in heterogeneous porous media due to the correlations provided by fractal distributions. These correlations include pore and throat size and shape, and their connectivity.

When implementing PNM, the initial step is to design the pore structure, which comprises the pores and their connectivity by throats (Martínez-Mendoza et al., 2019). The next step is to assign the phases in the medium and then the equations that describe the physical processes in the pore space. Overall, pore network models consist of five core concepts, which shall be discussed in this section. These concepts include the network, geometry, phases, physics and algorithms.

2.5.1 Network

The network is the description of the flow medium topology (Martínez-Mendoza et al., 2019). It represents the topology made of nodes/vertices (pores) and connections/edges (throats). In a porous media network model, nodes represent pores, and connections represent pore throats, as can be observed in Figure 2.9. The interconnectivity between the pores and pore throats within the rock structure is what creates the flow channels. The design of a network is the first step required while preparing a pore network model.

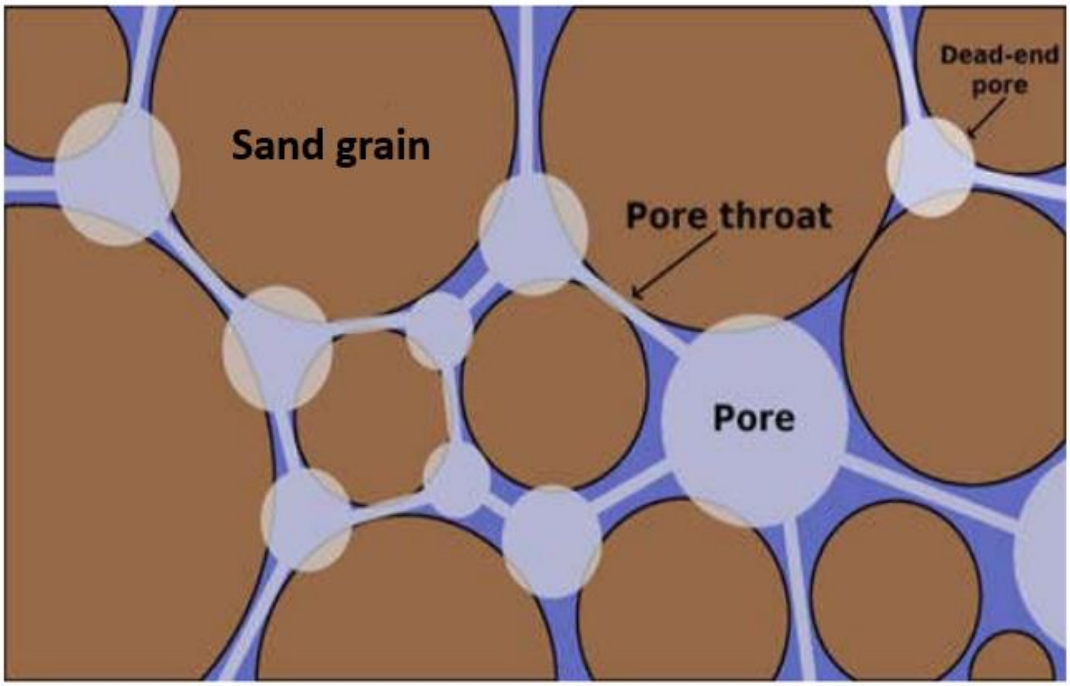

Figure 2.9 Representation of a pore network indicating the matrix (sand grain), pore and pore throat (Boccardo, et al., 2020). A dead-end pore appears when the pore is not connected to another throat.

2.5.2 Geometry

The geometry object defines the shape and size of the network's internal structures, such as pore & throat shape, diameters, and throat length (Martínez-Mendoza et al., 2019). The assigned geometry represents the shape of the pores and throats, respectively. To decide on the appropriate geometry to use, it is important to refer to the features of the rock under study. There are several research conducted to determine the pore and throat geometry of different rock types. For example, Gong et al. (2020) show that sandstones, both high and low porosity samples studied, have more triangular pores.

2.5.3 Phases

Upon defining the network topology and pore space geometry, the porous medium description is completed. The next step is to define the fluid(s) that may be occupying or flowing across the porous medium. The fluid can be in the liquid, gaseous or supercritical phase. The physical and chemical properties of the fluids can be described using correlations or equations.

2.5.4 Physics

Once the porous medium properties and the phases are defined, it is critical to account for the governing laws of physics. As fluid flows in a porous medium, properties such as capillary pressure, hydraulic conductance, and diffusive conductance come into play. The mathematical expression of physics is required for describing the nature of the transportation processes for calculating the related physical processes.

2.5.5 Algorithms

There are several algorithms embedded in pore-scale models for different purposes such as to simulate conduction, transport, and other multi-physics phenomena. Conduction algorithms, which include Fourier Conduction (Zhmakin, 2021) and Ohmic Conduction (Ovejas & Cuadras, 2018), often model heat or electricity conduction. These algorithms shall not be discussed in depth in this research. Transport algorithms such as Advection Diffusion, Fickian Diffusion, Invasion-Percolation, Drainage and Stokes Flow simulate mass, momentum, and energy transport in porous media (Jacob & Yehuda, 1990). Finally, multi-physics algorithms such as Reactive Transport model the interaction of several physical processes such as fluid movement, heat transport, and chemical reactions (Blazek, 2015).

Drainage algorithm (Yuan et al., 2015) simulates the invasion of a non-wetting phase into a porous medium saturated by a wetting phase. In this algorithm, fluid flow and phase distribution during the invasion are modelled, as well as the formation of capillary bridges and snap-off events. On the other hand, the **Invasion-Percolation** algorithm simulates the fluid invasion process as a series of events and traces the fluid movement as it invades the porous structure (Wilkinson & Willemsen, 1983). These two algorithms are suitable for relative permeability experiment simulation since they mimic the invasion process, account for the pore-scale geometry, and capture important phenomena such as capillary pressure, snap-off events, and hysteresis (Percolation and Clustering, 2002). However, unlike the Drainage algorithm, which is accurately applicable only to narrow pore size distribution, Invasion Percolation is applicable to a wider range of pore structures and flow conditions (Patzek, 2001).

Before describing invasion percolation theory in detail, it is imperative to start explaining the percolation theory itself. The term **percolation** refers to the gradual movement of substances in a medium. The percolation theory describes how clustered components behave in random networks (Grimmett, 1999). It is a common theory in Physics and Mathematics that has been used in practice to predict whether a component introduced on one end of a network will reach the other end and in what pattern. This probability theory was introduced since 1957 by Broadbent and Hammersley. However, the percolation theory utilises static properties of the flow medium despite it being intended to describe dynamic transportation in the media. Later, in 1982, Chandler et al. conducted a study on capillary displacement of two immiscible fluids and used the percolation theory to analyse the results. This study is what led to the introduction of invasion-percolation as a newer form of percolation theory.

The invasion-percolation model is a dynamic one contrary to the ordinary percolation model. In invasion-percolation, the displacement process is described at a constant flow rate rather than constantly applied pressure (Wilkinson & Willemsen, 1983). This feature makes it account for the trapping rule. Wilkinson and Willemsen

(1983) explain that the presence of deductible trapping in a network simulation is what differentiates invasion-percolation from ordinary percolation. When the simulation is run at a constant flow rate, it indicates a distinct time sequence of interface progress and, therefore, a distinct method of determining whether a certain portion of the displaced fluid becomes trapped or not. Under continuously applied pressure, on the other hand, the interface can advance in multiple places, and different time orderings might result in distinct trapping configurations.

To explain the ordinary percolation and invasion-percolation in a simpler-to-understand analogue, a lattice (Figure 2.10 a) will be considered as the flow medium. If a fluid is to be modelled to flow in the medium, the ordinary percolation algorithm will randomly assign sites (pores) or bonds (throats) that are wider thus, likely to be occupied by the fluid first, regardless of their location (Figure 2.10 b). These sites and bonds do not necessarily connect with each other. This is why the ordinary percolation theory is stated to be exhibiting more static properties. Nevertheless, an invasion-percolation algorithm will assign the fluid to flow into the widest sites and bonds to which the fluid can access at a certain point in time. This ensures a connected channel to be generated, establishing an inlet and an outlet for the fluid.

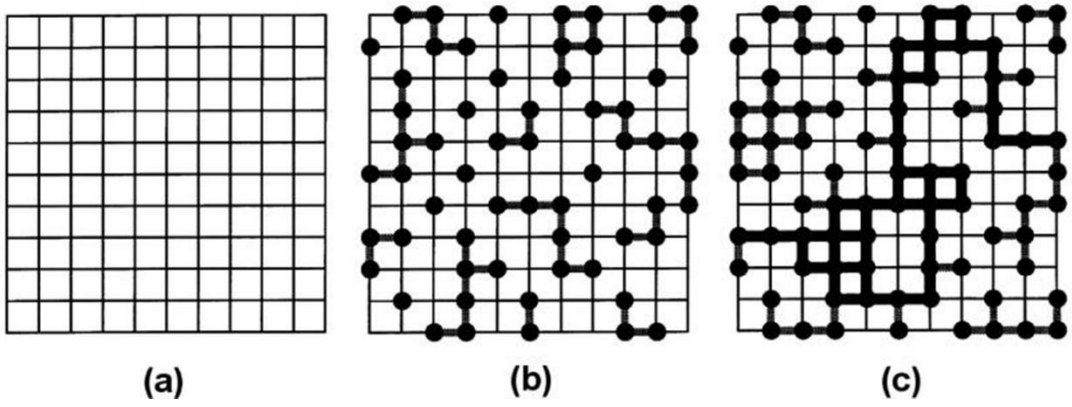

Figure 2.10 a) A regular square lattice, b) Ordinary percolation filled widest sites and bonds available in the lattice occupying 50% of the open space, c) Invasion percolation filled in the widest sites and bonds that came on the way from the inlet side (left) until it found its way on the other end (outlet, right). Observe how the dark thick line connects the channel from one end to another in a random pattern. (Berkowitz & Ewing, 1998).

Apart from modelling the mode of fluid flow in the porous medium, simulating viscous flow in a porous medium is another important aspect while conducting relative permeability experiments. This can be done using Stokes Flow algorithm. Stokes flow, also known as creeping flow, is a form of fluid flow where the inertial forces are negligible compared to the viscous forces (Trombley & Ekiel-Jeżewska, 2019). It is a type of flow common in porous materials due to the small sized pores as flow channels and the low velocities involved. Typically, this type of fluid flow has a low Reynolds number ($R_e << 1$) and is mathematically represented using Equation (2.9) and (2.10) for incompressible Newtonian fluids. Note that Equation (2.10) represents conservation of mass. Where u is the velocity field of a fluid, μ is the dynamic viscosity of the fluid, p is the fluid pressure field and ∇ is the gradient operator[2]. The Stokes Flow algorithm is designed to find the pressure distribution in the porous network, which then allows the calculation of fluid velocities.

$$\mu \nabla^2 u - \nabla p = 0 \tag{2.9}$$

$$\nabla . u = 0 \tag{2.10}$$

2.5.6 Extraction of Pore Network and Geometry from Real Porous Media

Before constructing pore networks, extracting pore space data that will be used in the network construction is imperative. Pore network information can be extracted in three common methods. These include imaging techniques, mercury intrusion porosimetry and gas adsorption which shall be briefly discussed. The networks can

[2] Gradient operator is a fundamental mathematical concept used in vector calculus to describe the rate of change of a scalar field in a multi-dimensional space. In the context of fluid dynamics and equations like the Stokes flow equation, the gradient operator is used to quantify how a scalar quantity (like pressure or velocity potential) changes with respect to spatial coordinates.

then be generated using the extracted data through different approaches, including image-based, regular network models, and grain-based methods. In this section, the techniques for pore space data extraction will be discussed, followed by the network construction techniques.

a) Imaging Techniques

In this method, high-resolution 3D images of the pore space are obtained using lab techniques such as X-ray, NMR, SEM etc. Then physical properties such as shape and size are assigned to construct a network of pores and throats that resemble the 3D image (Blunt et al., 2002). Figure 2.111 shows a digital image of a pore space from which the pore network was extracted to resemble its structure.

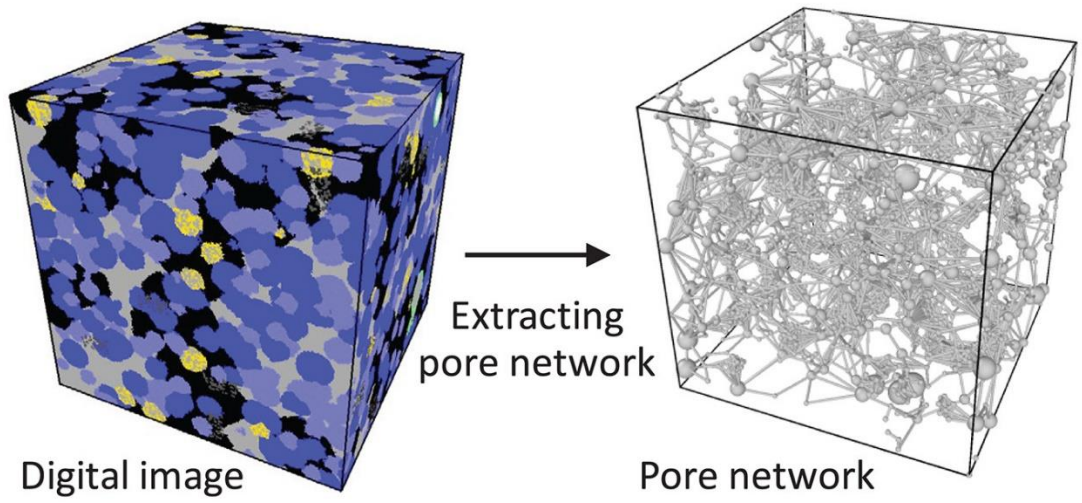

Figure 2.11 An illustration of a 3D pore space image converted into a pore network model (Wu, et al., 2019). The pore network model used spheres to indicate pores and cylindrical connections for throats.

There are two commonly used methods for representing pore spaces as 3D images for network extraction that will be discussed below:

- **Combining a series of 2D thin sections.** This is a commonly used core analysis method, although the process is strenuous. Holt et al. (1996) explain that this technique involves slicing rock and observing the grain structure under a polarizing or petrographic microscope. Figure 2.12 is an image of a 2D thin section and its binary image. The series of 2D visuals are then projected onto a computer connected to the microscope, where pictures are generated for every 10 μm to obtain a 3D pore space network (Holt et al., 1996).

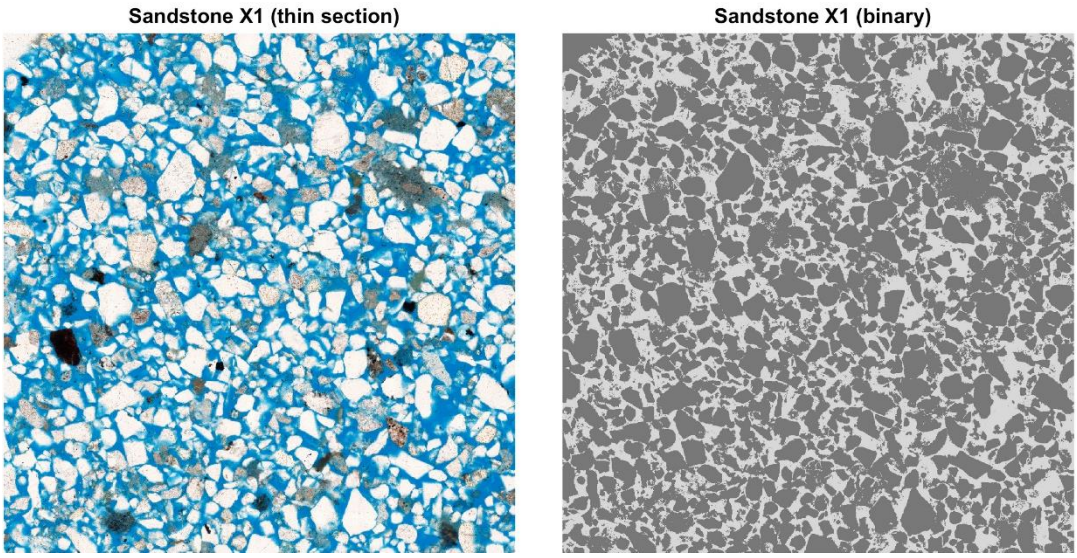

Figure 2.12 An example of a sandstone sample's a) 2D thin section and its b) binary image (Saxena, Mavko, Hofmann, & Srisutthiyakorn, 2017).

- **Using X-ray microtomography** (Dunsmuir et al., 1991). 3D images can be reconstructed from a stack of 2D slices using algorithms after their radiographic projections (Zhang et al., 2019) as represented by Figure 2.13. The high resolution obtained from this method increases the accuracy.

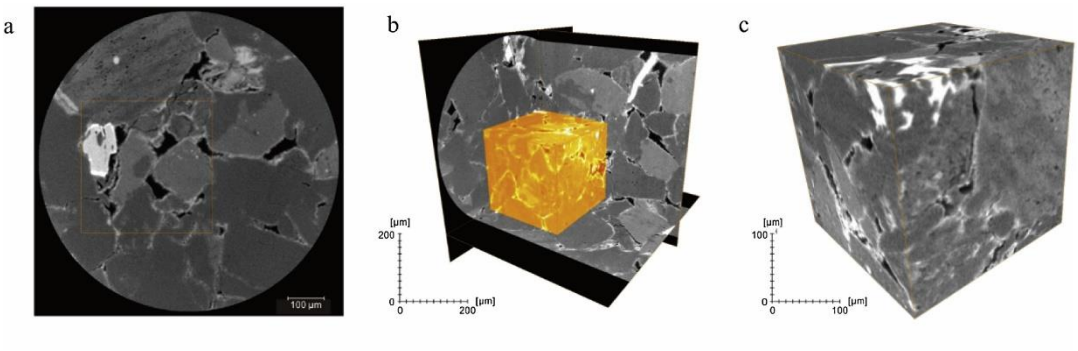

Figure 2.13 a) A 2D thin section tomography where the orange section is projected into a 3D representation shown in (b) and (c) (Zhang et al., 2019).

b) Mercury Intrusion Porosimetry (MIP)

The MIP method involves forcing mercury into pore spaces by applying pressure as high as 55,000 psi in order to determine the physical properties of the porous medium (Ozden, et al., 2018). It is a very useful method while studying media with pore throat sizes of between 500μm to 3nm (meso and larger macropores).

c) Gas Adsorption

The gas adsorption method functions in a similar fashion as MIP, except that it gives data on micropores smaller than 2nm (Wypych, 2017) and the analysis is based on the absorption characteristics of gases on solid surfaces (Fu et al., 2017). N_2, Ar and CO_2 are the commonly used gases for this method each suitable for different conditions.

2.5.7 Construction of Pore Network Models

While attempting to construct pore networks, one may use one of the existing three approaches. The first method involves the direct construction of a network from pore space images. The second approach involves the use of a lattice with certain pore coordination number and connectivity. The last approach involves simulating

geological processes to reconstruct the pore space. The three network generation approaches will be discussed in detail in this section.

a) Image-Based Construction

i. Direct Mapping

Upon obtaining the 3D images representing pore spaces, the network can be generated using several algorithms. This is generally done by indicating the pores and throats to create irregular pore network models. The following are the commonly used algorithms:

- **Erosion-dilation approach** – this algorithm extracts the networks from the images by running a skeleton through the centres of pores and throats (Gil & Kimmel, 2002). It is sometimes known as medial axis algorithm. The disadvantage of this method is its inability to differentiate between the pores and throats.
- **Maximal ball approach** – In this method, large spheres are used to represent pores, and small spheres represent throats (Arand & Hesser, 2017). This method may sometimes be unable to detect smaller elements in the image.

ii. Statistical Reconstruction

The analysis of 2D images representing pore spaces can be used to construct 3D images of the porous media. There are three levels of analysing 2D images of the porous matter: characterisation of the global properties, the morphology, and the topology (Leuitz, 2002). The first level, characterisation of the global properties, is the simplest and usually defines the porosity and the amount of interface per unit volume of the porous medium. The morphological analysis determines the average pore size, shape, surface roughness, mean curvature, and structural correlations between points belonging to the solid, the interface, or the pore network. Lastly, the topology establishes the connectivity of the pore network in the long range. To construct a more ordered-shaped pore network with physical properties resembling

the real network, the statistical reconstruction method has to be utilised (Hazlett, 1997). There are several statistical methods used to describe pore spaces, hence reconstructing the 3D networks. They include methods like truncated Gaussian random field (Adler & Thovert, 1998), a combination of one- and two-point correlation functions with some geometrical descriptors (Yeong & Torquato, 1998), stochastic method based on simulated annealing (Manwart et al., 2000), and multi-point statistical method (Okabe & Blunt, 2004).

iii. Two-Scale Pore Network Models

When constructing a pore network, the simultaneous characterisation of macro and micro properties is essential for the accurate simulation of classical empirical relations (Xiong et al., 2016). The models constructed by taking into account the porous medium properties at different length scales are referred to as the two-scale pore network models. One of the methods to generate such models proposed by Jiang et al. (2013) involves the integration of pore network models generated from images at different length scales. The excess number of network elements makes this method computationally costly. Another method by Mehmani & Prodanovic (2014) involves first constructing the macro-network, and then the generated network is downscaled to construct the microporous network. A two-scale pore network model is then constructed through packing algorithms.

b) Regular Network Model Construction Using Statistical Approach

Realistic pore networks are complex and difficult to construct. Regular pore network models are a simplified substitute which bases their properties on a wide range of statistical values obtained from real cores (Zhao et al., 2020). These models are usually defined by the connectivity, shape and spacing (OpenPNM, 2023). **Connectivity**, also known as coordination number, indicates the number of adjacent pores connected to a pore. The **shape** element defines the number of pores in each

direction (x, y, z) of the network. The **spacing** indicates the range of distance between pore centres in each direction.

The first regular network constructed is the cubic lattice, shown in Figure 2.14 (a), with a coordination number of 6 (Ioannidis & Chatzis, 1993). The cubic lattice by Ioannidis & Chatzis (1993) was used to match the porosity of the medium and simulate the drainage capillary pressure curves. This was later further advanced by Raoof & Hassanizadeh (2010) to a coordination number of up to 26 to have a more distributed connectivity, as seen in Figure 2.14 (b). The limitation of the higher coordination number is that throats intersect even on solid spaces (not pores only), which is far from reality. Other studies proposed structures such as the truncated octahedron with a maximum coordination number of 18 (Jivkov et al., 2013). Another structure which is less representative of the volume around the pore is the rhombic dodecahedron with a maximum coordination number of 12 and equal length throats (Vogel & Roth, 2001). Other regular network models include the Delaunay[3] and Voronoi[4] structures (Gostick, 2013).

[3] **Delaunay triangulation** is a geometric method used to divide a set of points into non-overlapping triangles, such that the circumcircle of each triangle contains no other points from the given set.
[4] **Voronoi diagram** is a type of tessellation pattern in which a number of points scattered on a plane is subdivided into exactly n cells enclosing a portion of the plane closest to each point.

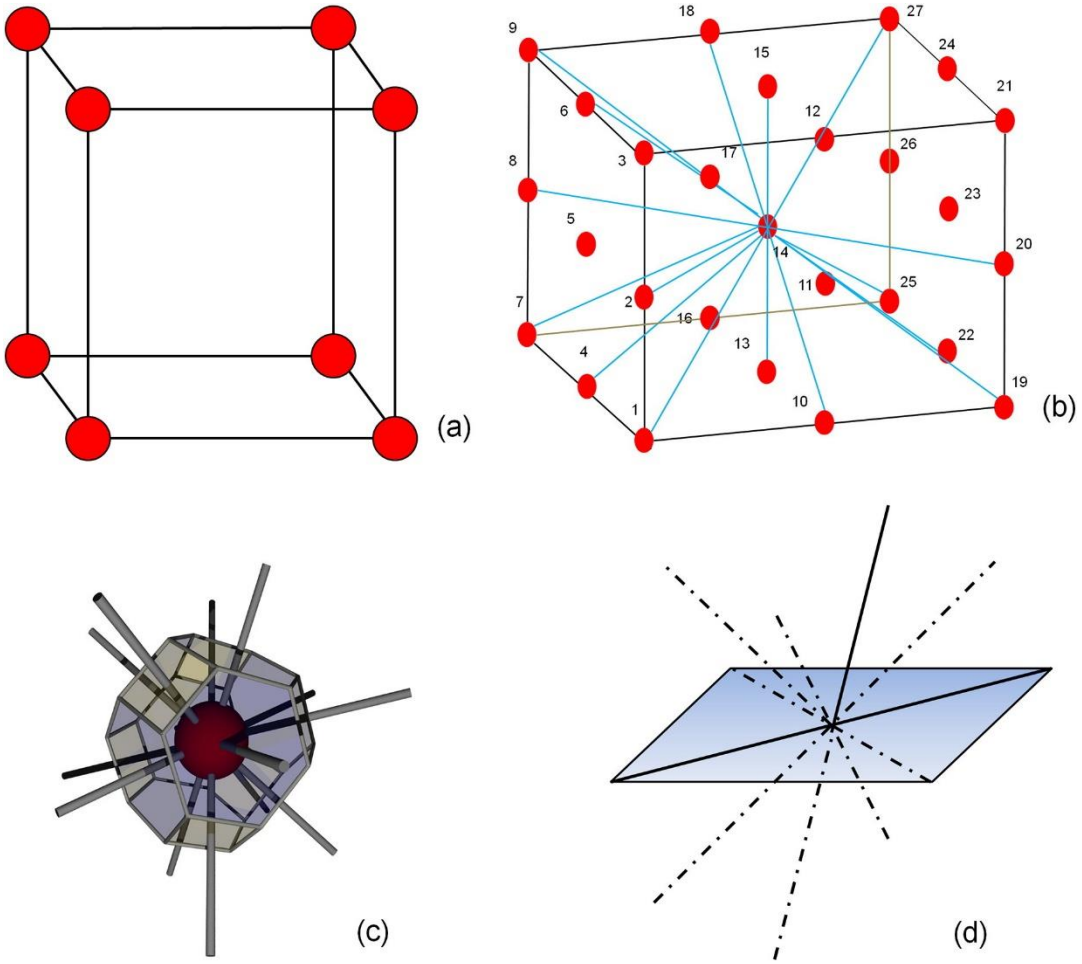

Figure 2.14 Regular network models: a) a basic cubic lattice with a connectivity of 6, b) a cubic lattice with a connectivity of 26, c) truncated octahedron, and d) rhombic dodecahedron (Xiong et al., 2016).

c) Grain-Based Model

This approach entails simulating the geological processes that formed the porous medium to reconstruct it as seen in Figure 2.15 (Xiong et al., 2016). It involves packing spheres of equal (Bryant et al., 1993) or different (Øren et al., 1996) sizes

together and simulating diagenesis and compaction processes. Diagenesis[5] is simulated by enabling the spheres to swell and overlap. Compaction[6], on the other hand, is modelled by shifting the spheres' centres closer together in the vertical direction, causing them to overlap. The geological reconstruction should ideally describe the pore geometry and topology correctly and depicts the connectedness of the rock, as proven by Øren & Bakke (2002). This strategy, however, may not be appropriate for complex systems incorporating sedimentary processes, microporosity, and clays.

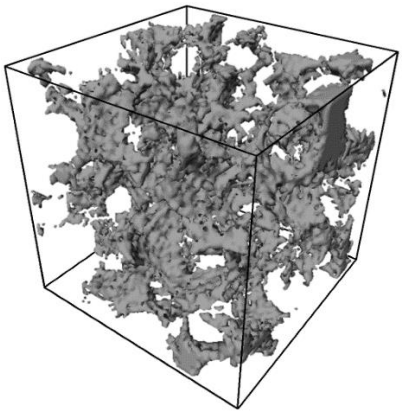

Figure 2.15 A representation of a 3D porous medium reconstructed by simulating the geological processes (Øren et al., 1996).

2.6 Previous Studies on CO_2-Brine Relative Permeability

In reservoir engineering, relative permeability experiments have been conducted for years mostly using oil and water (or air and water) as the flowing phases. The

[5] **Diagenesis** is a process describing physical, chemical and biological changes that affect sedimentary rock properties after deposition (Milliken, 2003).
[6] **Compaction** happens when sediments are pressurized due to being buried deep underground (Chapman, 1983). It is part of the lithification process.

advancement of CO_2 for EOR ignited the early research on three phase relative permeability for oil-water-CO_2 (Fayers et al., 1981). Later on, relative permeability tests for CO_2 against other fluids were conducted for integrated EOR and CCS projects (Moodie et al., 2019, Sedaghatinasab et al., 2021, and Kashkooli et al., 2022), and some solely for geological sequestration. Table 2.1 shows a list of select research whose objective is to determine CO_2-brine relative permeability experimentally. Below Table 2.1 is Table 2.2, which shows computer-based experiments, particularly pore network modelling, for determining CO_2-brine relative permeability.

`

Table 2.1 Summary of previous research papers on CO_2-brine relative permeability laboratory-based experiments.

Author(s)	**Approach**	**Lithology**	**P-T Conditions & Phase**	**Critical Findings**
Chalbaud, et al. (2007)	Unsteady state	Carbonate	10 MPa, 60℃ Supercritical	• If CO_2 is the non-wetting phase, performing experiments at reservoir conditions to obtain k_r and P_c is unnecessary. • Partial wetting by the CO_2 causes a lower capillary BT pressure hence decreasing reservoir CO_2 storage capacity.
Bennion & Bachu (2008)	Unsteady state	Sandstone and carbonate	8.6-27 MPa, 35-75˚C Supercritical	• Less concave k_r curves for higher median pore size indicating decreased multiphase interference effects. • Corey exponents for k_r curves are higher for gas than brine phase.
Akbarabadi & Piri (2013)	Steady and unsteady state	Sandstone	3.45-11 MPa, 20-55˚C Supercritical and gaseous	• Capillary forces can trap a significant amount of injected CO_2. • For a given initial brine saturation, residual saturation for gaseous CO_2 is higher than for sc.
Chen et al. (2014)	Steady state	Sandstone	10.3 MPa, 20˚C Liquid	Compared to previous studies: • During CO_2 drainage, CO_2 had a higher k_{rgcw} and nearly constant k_{rw}. After CO_2 drainage, a higher max. S_g was obtained. • After brine imbibition, higher S_{gr} and similar S_g decrease was found.
Bakhshian et al. (2020)	Steady state	Sandstone	34.47 MPa, 122˚C Supercritical	• Directional variability is important to consider for accurate k_r prediction. For horizontal samples, k is controlled by the highly permeable layers and for vertical it is the low permeable layers controlling k.
Moore et al. (2021)	Unsteady state	Sandstone, carbonate, and basalt	9.65 MPa, 63.3˚C Supercritical	• Steady state experiments achieve more drainage of wetting brine as compared to unsteady state ones. • Steady state tests demonstrate a larger slope of the curve fits due to availability of data at the higher and lower saturations. • $scCO_2$ and brine unsteady-state k_r approximates real-world injection conditions better.

Table 2.2 Summary of previous research papers on CO_2-brine relative permeability using pore network modelling.

Author	**Network/Geometry**	**Findings**
Lopez et al. (2011)	Network and geometry data imported from 3D digital images of sandstone samples from In Salah, Algeria.	• PNM results similar to experimental in terms of shape and endpoints. • The relative permeability end-points can be correlated with the geometry, topology and morphology of the rock pore space.
Varloteaux et al. (2013)	Network and geometry data imported from 3D digital images of Fontainebleau sandstone.	• The relative permeability measurements corresponded to Corey correlations.
Wang et al. (2016)	Network extracted using the Maximal Ball (MB) Algorithm on CT images of methane hydrates.	• Under the same S_w, a larger k_{rw} and lower k_g observed on hydrate-bearing porous media formed with larger-size particles.
Mutailipu et al. (2017)	Networks of 4 samples (Quartz, Dolomite, Feldspar, Berea) extracted from digital images using the Maximal Ball (MB) Algorithm.	• Samples with similar pore structures exhibit similar relative permeability curves. • Temperature and pressure change do not affect drainage cycle but affects the imbibition cycle where k_g decreases with increasing pressure and temperature.
Kohanpur et al. (2020)	Network extracted using the Maximal Ball (MB) Algorithm on 3D digital images of a heterogeneous sandstone sample, Mt Simon.	• Relative permeability results using LB, DNS and PNM are agreeable. The difference is computational power and time.
Hefny et al. (2020)	Network extracted from X-ray Tomographic 3D images of a Nubian Sandstone rock.	• The relative permeability curves correspond to experimental ones on the same rock. • A land trapping coefficient of 1.2 obtained and can estimate the extent of CO_2-plume migration.

2.7 Comparison of PNM to Experimental/Analytical Results in the Literature

Table 2.2 has shown that most research conducted on CO_2-brine relative permeability using pore network modelling compared their results to either previous experimental results, empirical models (such as Corey models) or other computer simulation methods. In this section, some graphs selected from literature making these comparisons will be shown and briefly discussed.

Figure 2.16 compares PNM generated results by Mutailipu et al. (2017) against experimental results from Perrin et al. (2007). The CO_2-brine relative permeability simulation on Berea sandstone was conducted at 323 K and 12.4 MPa using 6 g/L NaCl solution. A good correlation between PNM and experimental results can be observed. Another comparison is shown in Figure 2.17 where Lopez et al. shows results obtained from experiments labelled as 'Core' and PNM results labelled as 'LET-JIP'. Both the core samples used in experiment and the modelled ones are from the same carboniferous sandstone reservoir in Algeria but with slight differences in depth, porosity and permeability.

Figure 2.18 shows the comparison between PNM generated results against Corey correlation. Equation (2.11), (2.12) and (2.13) are the modified Brooks-Corey expressions for water, oil, and gas relative permeabilities respectively where all the terms are as given in the list of symbols and n is the exponent value unique to each fluid (PetroWiki, 2016). The equations are also known as the "Power-law" relationships and are used to describe how different phases of fluid flow through porous media under different saturation conditions in reservoir engineering (Brooks & Corey, 1964). The Pore Network Model by Varloteaux et al. (2013) uses the network extracted from 3D-images of Fontainebleau sandstone.

$$k_{rw} = k_{rw,max}\left(\frac{S_w - S_{wc}}{1 - S_{or} - S_{wc} - S_{gc}}\right)^{n_w} \tag{2.11}$$

$$k_{ro} = k_{ro,max}\left(\frac{S_o - S_{or}}{1 - S_{or} - S_{wc} - S_{gc}}\right)^{n_o} \tag{2.12}$$

$$k_{rg} = k_{rg,max}\left(\frac{S_g - S_{gc}}{1 - S_{or} - S_{wc} - S_{gc}}\right)^{n_g} \tag{2.13}$$

One more literature comparison to observe is by Kohanpur et al. (2020) shown in Figure 2.19. They compared the PNM results generated for Mt. Simon sandstone to those generated using Direct Numerical Simulation and Lattice Boltzmann method.

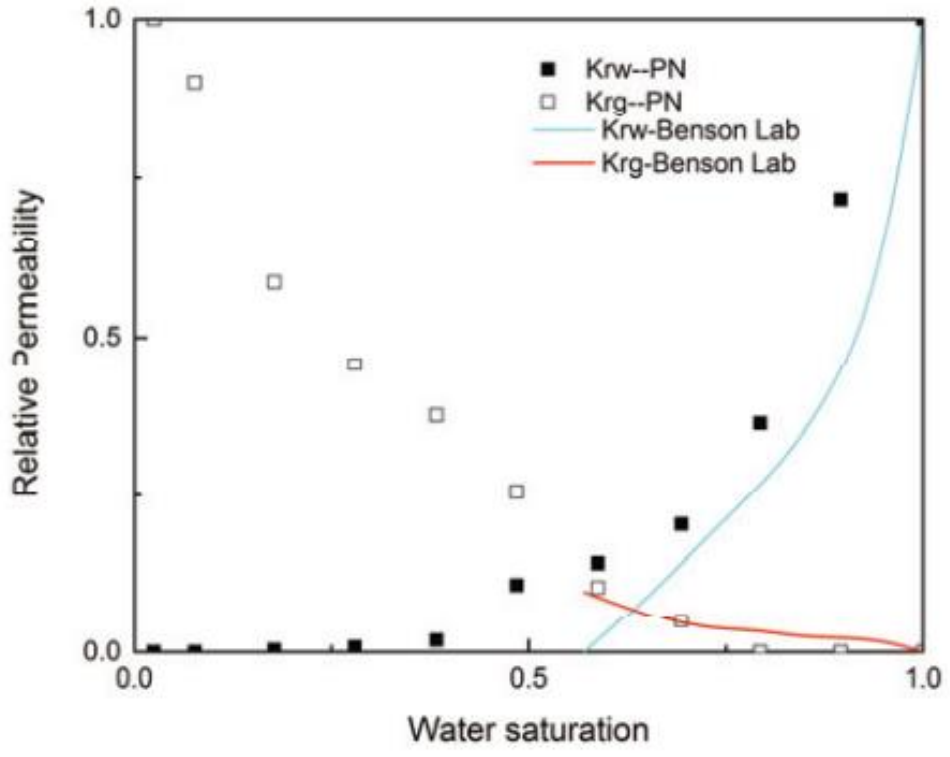

Figure 2.16 Comparison between Mutailipu et al.'s PNM based CO_2-brine relative permeability against Benson Lab's results on Berea sandstone (Mutailipu, et al., 2017).

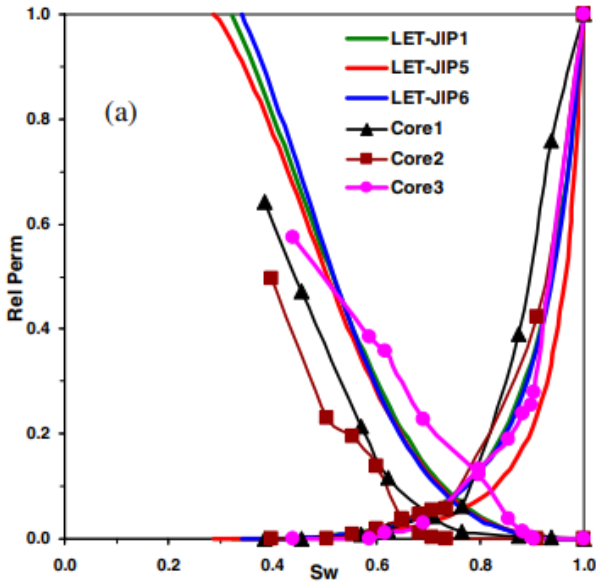

Figure 2.17 Comparison between Lopez et al.'s PNM based CO_2-brine relative permeability against their experimental results for a sandstone sample from Algeria (Lopez, et al., 2011).

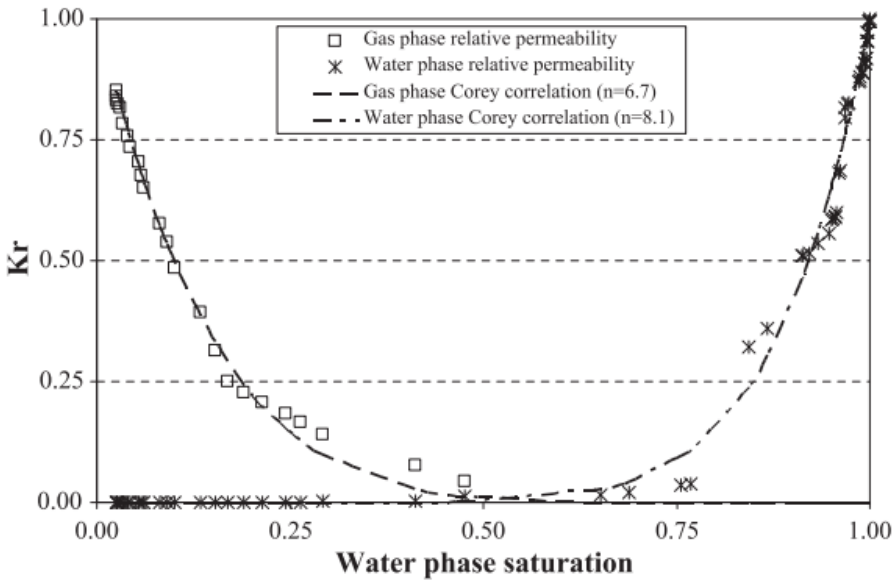

Figure 2.18 Comparison between Varloteaux et al.'s PNM based CO_2-brine relative permeability against Corey correlation results for Fontainebleau sandstone (Varloteaux et al., 2013).

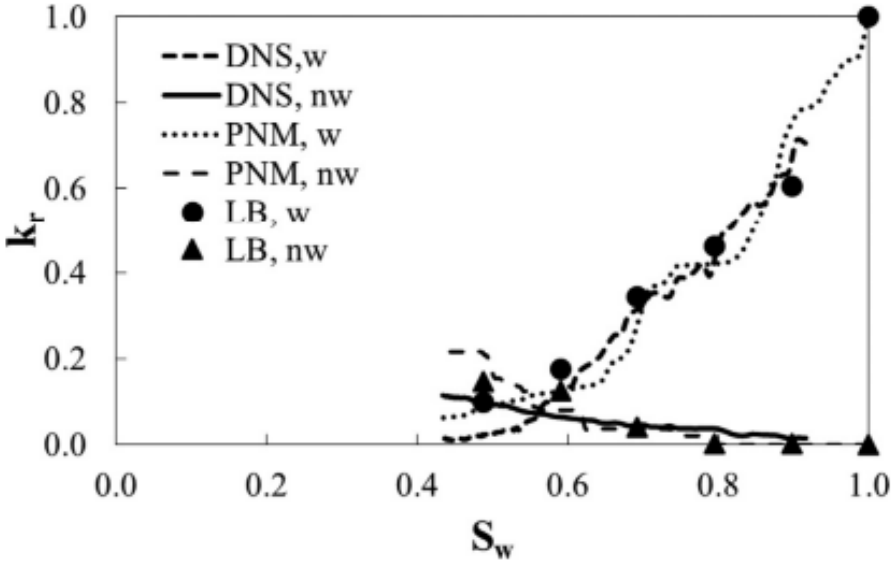

Figure 2.19 Comparison between Kohanpur et al.'s PNM based CO_2-brine relative permeability against Direct Numerical Simulation and Lattice Boltzmann results for Mt Simon sandstone (Kohanpur et al., 2020).

CHAPTER 3

METHODOLOGY

Before describing the methodology used in this research in depth, it is important to highlight that the first chosen methodology was experimental. A traditional steady state and unsteady state coreflooding experiment was to be conducted using brine and gaseous CO_2 at certain temperatures and pressures to resemble existing literature conditions for comparison. Later, this was changed to the newly introduced method, the intercept method which was explained in Section 2.4.1 due to the simplicity of its execution in the experimental step. However, eventually the methodology was altered to using computer based modeling due to lack of suitable equipment. As stated in different research papers (Khaz'ali et al., 2011, Arigbe et al., 2019, Wang at el., 2019, and Acharya et al., 2023), relative permeability experiments are time-consuming and expensive to conduct. Therefore, the focus here will be on the easily accessible method, pore network modelling using the open source: OpenPNM.

3.1 Overview of Pore Network Modelling Technique Used (OpenPNM)

OpenPNM is a pore network modelling package with a readymade framework for performing relative permeability simulations (Gostick, et al., 2016). It is an open-source python package making it freely and easily accessible. Figure 3.1 shows a summary of steps required to perform pore network modelling in OpenPNM.

To perform pore network modelling in OpenPNM, the first step is to import the libraries. The next step is to design the pore network model by assigning the network and geometry properties. The most common network is the cubic lattice which can also be used as a template to design arbitrary shapes like spheres or cylinders. Random networks may also be designed in OpenPNM using the Delaunay and Voronoi Tessellations. The shape size, spacing and connectivity are among the

topological features that can be adjusted in the OpenPNM built model. The connectivity ranges from 6-26 connections with 6 as the default and if spacing is not specified, it is assumed to be [1, 1, 1]. The network can also be imported from Porespy which extracts pore networks from high resolution 3D images of pore spaces. In this research, a simple cubic lattice was used as it is the preferred model in literature due to its simplicity and sufficiency. The shape, spacing and connectivity varied based on the properties of the sample being replicated.

The geometrical properties such as pore and throat shape and size can then be assigned to generate the desired network. OpenPNM has several geometry modules such as spheres and cylinders, cubes and cuboids, and circles and rectangles and a few others standing for the pores and throats shapes. The other main geometric properties defining the network are physical sizes of pores and throats including pore and throat diameters and lengths. The geometrical parameters may be manually assigned to the network, but it is easier to use existing models form the library. The initial plan was to assign the shape of the pores and throats that corresponds to the respective lithology based on literature findings. For example, Gong et al. (2020) found that sandstone formations mostly had triangular shaped pores. However, after running several simulations with different geometry modules, the results were found to be within the same range. Therefore, the module spheres and cylinders were chosen as it is the most used one in pore scale network modelling research papers.

Upon generating the network with its geometrical properties, assigning the phases follows. For relative permeability experiments, wetting and non-wetting phases are assigned. OpenPNM has its own library for some common fluids like air, water, and mercury. For other fluids, one may use one of the suitable classes that OpenPNM hosts and if required, define the properties of the phases. Some of these classes include Species, Mixture, Standard Gas, Liquid Mixture, and Binary Gas. Since the phases used in this research, brine as wetting and CO_2 as non-wetting, did not correspond to any of the classes with a built-in model for calculating their properties, the class Phase which produces an empty object was used. Then the required fluid properties, like density, viscosity, and IFT for computing relative permeability were

manually added. Since it was assumed that the core would have a constant temperature, the viscosity of the fluids is not expected to change.

If this was a laboratory experiment, it can be said that so far, the experimental setup along with the core sample and fluids, has been set. The pore network model designed using network and geometry elements correspond to the core sample, and the phases have been assigned. The next step would be to define the governing physical processes which restrict or assist the transport process. This step would aid to bring the model to life by imitating natural conditions. OpenPNM includes physical processes like conductance, capillary effects and reaction rates. In the created model, multiphase conductance was assigned to account for the effect of one phase over another for effective permeability calculations.

Upon defining the physics involved, the mode of fluid flow in the pore space along with its associated processes, will be determined. In pore network modelling terms, the algorithm has to be assigned. The classes of algorithms in OpenPNM include advection diffusion, reactive transport, ohmic conduction and Fickian diffusion. To conduct relative permeability experiments, invasion-percolation and stokes flow algorithms were used. Invasion-percolation was used for obtaining the invasion sequence during coreflooding (state of pore saturations at a given overall saturation). Stokes flow, on the other hand, since it describes the flow of incompressible fluids, was used when calculating the flow rate of the phases at a given overall saturation. These two algorithms are explained in detail in Section 2.5.5.

The last step before running the model, is adding the computational functions. In this step, functions are added to calculate the required parameters like absolute permeability and saturation. Typically, custom functions are created to calculate a certain property. In the created model, custom functions were used to calculate the fluid saturations and relative permeability values for specified number of overall saturation values. Then a plot was generated using the obtained sets of data.

One important feature that pore network modelling embodies is ability to visualize the designed network. For OpenPNM, visualization can be done using the two

common environments: Jupyter Notebook and Spyder or using Paraview. Paraview is a separate open-source visualization software that could be used for better quality images. OpenPNM allows the pore network files to be saved in different formats. The appropriate format (vtp) can be exported directly to Paraview for higher resolution visualization.

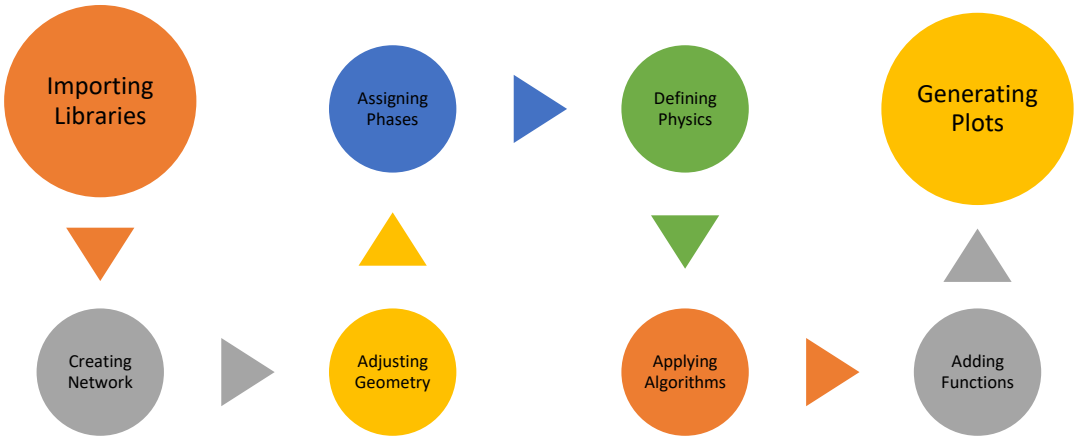

Figure 3.1 Summary of steps used in OpenPNM to perform pore network modelling simulations.

3.2 Data Acquisition and Input Parameters for the Simulations

The data was chosen from previous CO_2-brine relative permeability experiments in the literature to compare the results. Statistical reconstruction of the pore network models was done using the distributions or mean values for properties like pore and throat sizes. Several rock samples of different lithology were used. These samples

include Berea[7] sandstone, Mt Simon[8] sandstone, and a carbonate sample. Overall, for each sample under study, the following data will be obtained:

- Pore and throat size distributions
- Average connectivity/coordination number
- Average porosity
- Fluid properties (density, viscosity, contact angle, interfacial tension)

Berea Sandstone

This sample is fairly homogenous in nature with well-sorted and well-rounded sand grains (Churcher et al., 1991). Additionally, it contains small amounts of feldspar, dolomite, and clays. This sample is among the most commonly used ones in literature due to its accessibility. It covers most of the Appalachian basin (Potter et al., 1984). Øren & Bakke (2003) reconstructed the sample's 3D images using 2D thin section images to extract petrographical properties. From their study, the pore and throat size distribution, and the coordination number distribution were obtained. However, since this study was focused on comparing the results to experiments that used CO_2-brine, Øren & Bakke (2003) was not preferred since they used oil-water-gas. Rather, the network properties are from Mutailipu et al. (2017), whose results could be compared to this study. Mutailipu et al. (2017) presented the properties of the pore networks extracted from the samples as average values instead of a distribution. Table 3.1 shows the pore network properties of Berea sandstone presented in that paper.

[7] Berea is a 72-79 m thick sandstone formation from Michigan, Ohio, Pennsylvania, West Virginia, and Kentucky in the U.S.
[8] Mt Simon is a sandstone formation from Illinois, Indiana, Kentucky, Michigan, Minnesota, Ohio, and Wisconsin in the U.S with thickness of up to 610 m.

Table 3.1 Average pore network properties extracted from Berea Sandstone sample by Mutailipu et al. (2017).

Property	**Value**
Porosity (%)	26.32
Average coordination number	3.35
Average pore radius (10^{-6}m)	19.2
Average throat radius (10^{-6}m)	9.08

The properties of the wetting (brine) and non-wetting (CO_2) phases used when running the Berea sandstone network simulation have also been given by Mutailipu et al. (2017). These properties are given in Table 3.2.

Table 3.2 Fluid properties for the wetting and non-wetting phases used in the Berea sandstone sample used by Mutailipu et al. (2017).

Property		**Value**
Pressure (MPa)		12.4
Temperature (K)		323
Non-wetting phase	Density (kg/m^3)	607.85
	Viscosity (cP)	0.046
Wetting phase	Density (kg/m^3)	997.38
	Viscosity (cP)	0.555
Interfacial Tension (mN/m)		26.8
Contact Angle (degrees)		50˚

Mt Simon sandstone

Another sample also commonly used in several experimental work is Mt Simon sandstone from the Upper Cambrian period. This sample has been used by Kohanpur et al. (2020) in their study for analysing two phase flow of CO_2 and brine using pore network modelling. The data used will be replicated in our study to compare the results. Figure 3.2 gives the pore and throat size distribution and Table 3.3 gives the fluid properties. Additional important data that is not included includes the average connectivity of the sample which is estimated as 5 connections and the porosity of 26.3%.

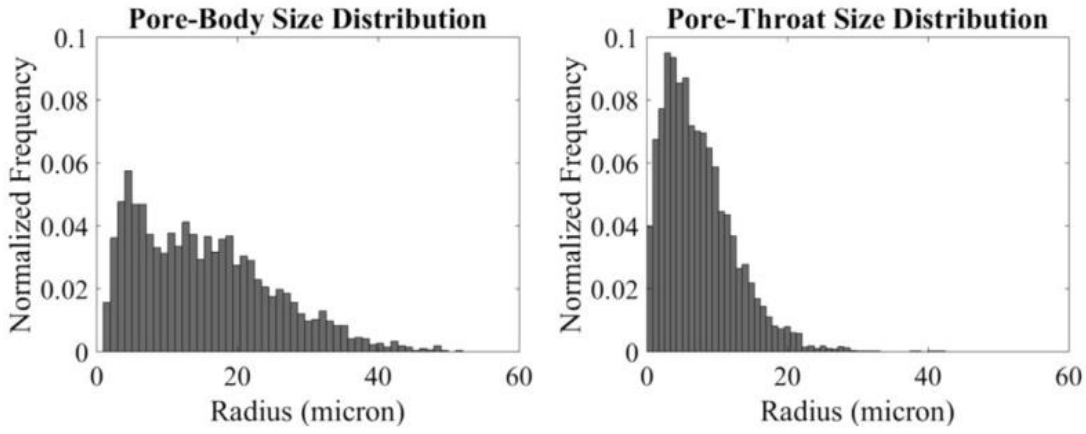

Figure 3.2 Pore and throat size distributions for Mt Simon sandstone sample (Kohanpur, Rahromostaqim, Valocchi, & Sahimi, 2020).

Table 3.3 Fluid properties for the wetting and non-wetting phases used in the Mt Simon sandstone sample obtained from Kohanpur et al. (2020).

Property		**Value**
Non-wetting phase	Density (kg/m^3)	1100
	Kinetic Viscosity (m^2/s)	1×10^{-7}
Wetting phase	Density (kg/m^3)	1100
	Kinetic Viscosity (m^2/s)	1×10^{-6}
Viscosity Ratio		10
Interfacial Tension (mN/m)		30.0
Contact Angle		180˚

Carbonate

Apart from the 2 sandstone samples, a carbonate sample is also studied due to its different interaction with the fluids. A cretaceous carbonate sample obtained from subsurface Oman studied by Al-Kharusi and Blunt (2007) was chosen due to data availability. The sample's pore throat size distribution is shown in Figure 3.3. Since the distribution has triple modal, the carbonate could be a Calcite, dolomite, or pyrrhotite (Miaomiao et al., 2022). Fluid properties for the sample were provided in another paper by the same authors which was published a year later (2008) using the constructed network (Table 3.4). The average porosity and connectivity are given as 33.3% and 5 connections respectively (Al-Kharusi & Blunt, 2007).

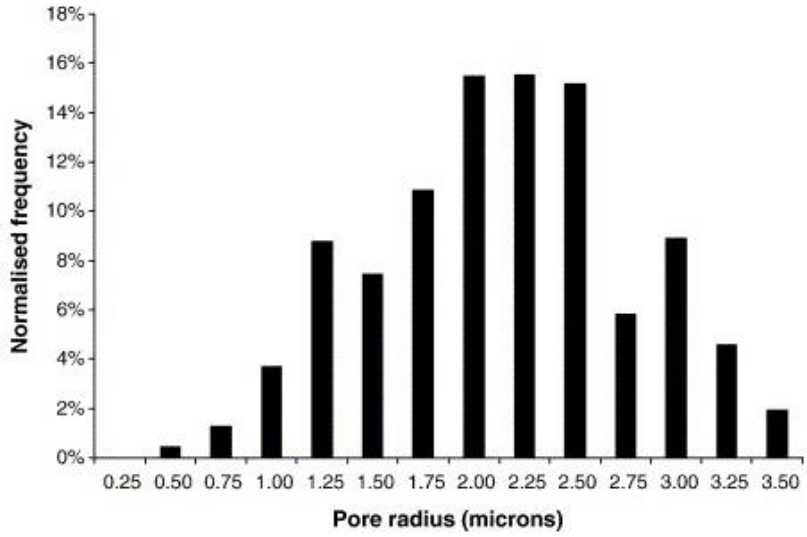

Figure 3.3 Pore throat size distributions for a carbonate sample obtained from Al-Kharusi & Blunt (2007).

It is important to note that, even though Al-Kharusi & Blunt (2007) labelled Figure 3.3 as pore size distribution, it is supposed to be pore throat size distributions. The small radii are more representative of pore throat sizes as can be commonly observed in different literature (Li, et al., 2020), (Liu et al., 2022) and (Miaomiao et al. 2022).

Table 3.4 Fluid properties for the wetting and non-wetting phases used in the carbonate sample obtained from Al-Kharusi & Blunt (2008).

Property		**Value**
Non-wetting phase	Density (kg/m^3)	782
	Viscosity (mPa.s)	1.4
Wetting phase	Density (kg/m^3)	1098
	Viscosity (mPa.s)	0.66
Interfacial Tension (mN/m)		22.5
Contact Angle (degrees)		30˚

3.3 Absolute Permeability Calculation Data

In Section 2.2, the Kozeny-Carman Equation (2.2) which is a theoretical relationship for estimating absolute permeability of a porous medium was discussed. This equation, which uses geometric properties of a porous media, was coupled with a relationship derived by Kamann et al. (2007). Equation (3.1) represents the relationship to obtain the average diameter of sand grains (d_g) using the average diameter of pores (d_p) (Kamann et al., 2007).

$$d_p = 0.414 d_g \tag{3.1}$$

To calculate absolute permeability using Kozeny-Carman equation, pore geometry data used in OpenPNM was obtained. The sphericity was assumed as 1 to match the spherical pores used in OpenPNM. Table 3.5 shows the porous media data for the 3 samples used in this study. The network properties for the samples used in OpenPNM are as shown in Table 3.6.

Table 3.5 Pore Space Geometry data for three samples obtained from OpenPNM model.

Sample	**d_p (micron)**	**Φ**
Berea	38.4	0.28
Mt Simon	30.5	0.21
Carbonate	2.02	0.21

Table 3.6 Network properties for three samples as used in the OpenPNM model.

	Size	**Spacing (m)**	**Connectivity**	**Dimensions (m^3)**
Berea	(40, 40, 40)	2.1×10^{-6}	18	$(8.4\times8.4\times8.4)10^{-15}$
Mt Simon	(40, 40, 40)	2.9×10^{-6}	26	$(1.2\times1.2\times1.2)10^{-12}$
Carbonate	(40, 40, 40)	1.5×10^{-8}	26	$(6\times6\times6)10^{-21}$

CHAPTER 4

RESULTS AND ANALYSIS

4.1 Comparison of OpenPNM Absolute Permeability Results with Kozeny-Carman

Before discussing two phase flow results, single phase flow results will first be presented. Table 4.1 shows the absolute permeability values obtained from literature PNM, OpenPNM (our model) and Kozeny-Carman calculated values. The Kozeny-Carman model results are used to validate[9] our model. Initially, the spacing value used in our OpenPNM model for all samples was 1×10^{-5} m. This generated extremely high values that were not close to Kozeny-Carman calculated values. Upon adjusting the spacing, absolute permeability values close to those calculated using Kozeny-Carman empirical equation were obtained. Changing the spacing had no effect on porosity or relative permeability, it was beneficial to adjust the model to have absolute permeability values that matched Kozeny-Carman with lower % error.

[9] **Model Validation** is a process of determining the degree to which a computer model is an accurate representation of the real world. On the other hand, **model verification** is the process of determining that a model implementation accurately represents the developer's conceptual description of the model and its solution (Thacker, et al., 2004). In this research, we try to validate our model.

Table 4.1 Absolute permeability values for three samples obtained from three different methods.

Sample	Kozeny-Carman (mD)	Literature PNM (mD)	OpenPNM (mD)	Spacing (m)	% Error K-C vs OpenPNM
Berea	2050	191,808	2048	2.1×10^{-6}	0.10%
Mt Simon	453	4,201	455	2.9×10^{-6}	0.44%
Carbonate	1.96	2.4	1.98	3.0×10^{-8}	1.02%

4.2 Determining the CO_2 Phase for each Simulation

Based on the temperature and pressure conditions, the CO_2 phase is expected to change as shown in Table 4.2 and marked on Figure 4.1. The assigned conditions are replicated as the studies that this work is comparing to.

Table 4.2 CO_2 phase used in the three samples based on the temperature and pressure conditions of the simulations.

Sample	Pressure (MPa)	Temperature (K)	CO_2 Phase
Berea	12.4	323	Supercritical
Mt Simon	0.101	298	Gaseous
Carbonate	27	393	Supercritical

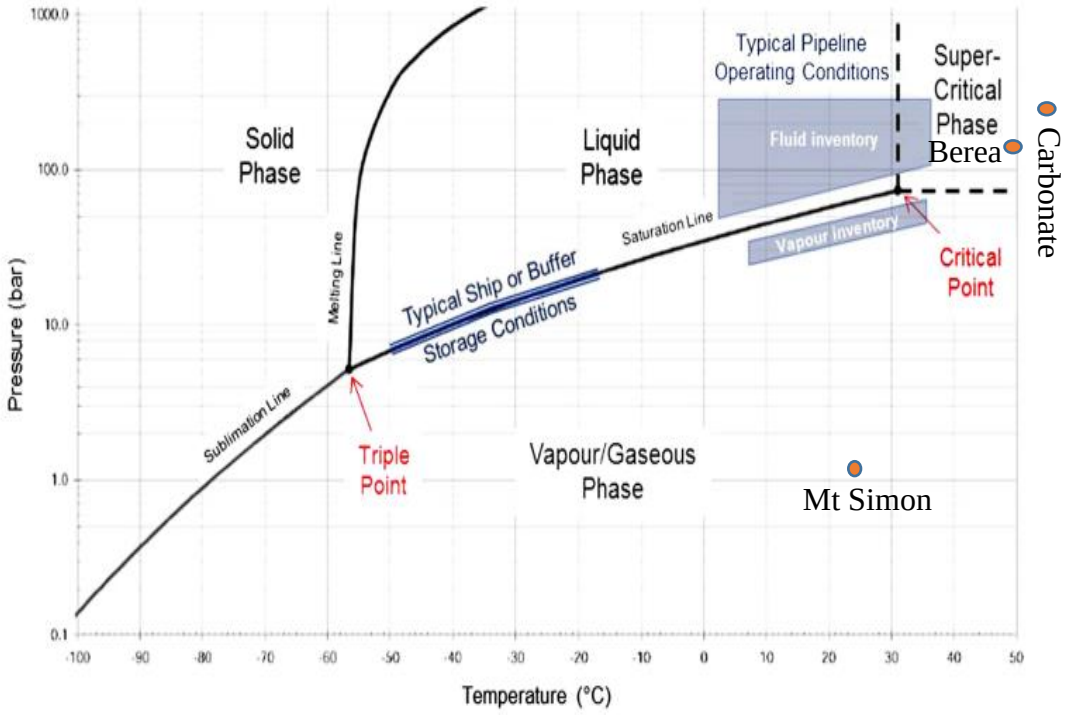

Figure 4.1 CO_2 phase for Berea, Mt Simon and Carbonate samples on the phase diagram.

4.3 Comparison of OpenPNM Relative Permeability Results with Other Results from the Literature

As discussed in Chapter 3, three samples whose data could be obtained in literature were used to verify the accuracy of the utilized method. The samples are Berea sandstone, Mt Simon sandstone and a carbonate rock from subsurface Oman. The results obtained using OpenPNM, were compared to other pore network modelling results and lab experiment results where available. In this section, the results obtained for each sample will be discussed and compared while analyzing the discrepancies in the results.

Berea Sandstone

The experiment results are from a drainage test conducted on a sample that was initially fully saturated with brine. The relative permeability curve obtained for Berea sandstone was a smooth curve with an error[10] of 18% from the study compared, as can be seen in Figure 4.2 and Figure 4.3. The following are the important points to note from the results:

- **Porosity:** the porosity of the network generated in OpenPNM was 28% which is close to that of the compared study-26% with an error of around 7.7%.
- **Wettability[11]:** the intersection point of the curves is inclined towards the right of the plot. This indicates that the results obtained imply a more water-wet medium similar to the results of the study it is compared to. Additionally, the crossover point from OpenPNM, is very close to that from the experimental study.
- **Residual saturation:** the residual saturation of the wetting phase obtained using OpenPNM is similar to that from the experiment, around S_{wi}=0.58. The literature PNM wetting phase residual saturation value deviates from the experiment value by 34.5%. However, the residual saturation for the non-wetting phase is closer to the PNM results from the literature than the experiment, S_{rg}=0.2. The PNM non-wetting phase residual saturation value deviates from the experiment value by 19%. The OpenPNM invasion-percolation algorithm was run for a drainage experiment, hence CO_2 initial saturation being 0 is more accurate for the situation. However, the PNM relative permeability curve taken from literature represents an imbibition test.

[10] The average error calculation is explained in the appendix

[11] In OpenPNM using invasion percolation, an invading fluid is assigned. The other fluid is then assumed to be the one initially occupying the core and is the wetting phase. Additionally, if the contact angle is assigned, the wettability defined by the contact angle value redefines the wetting phase.

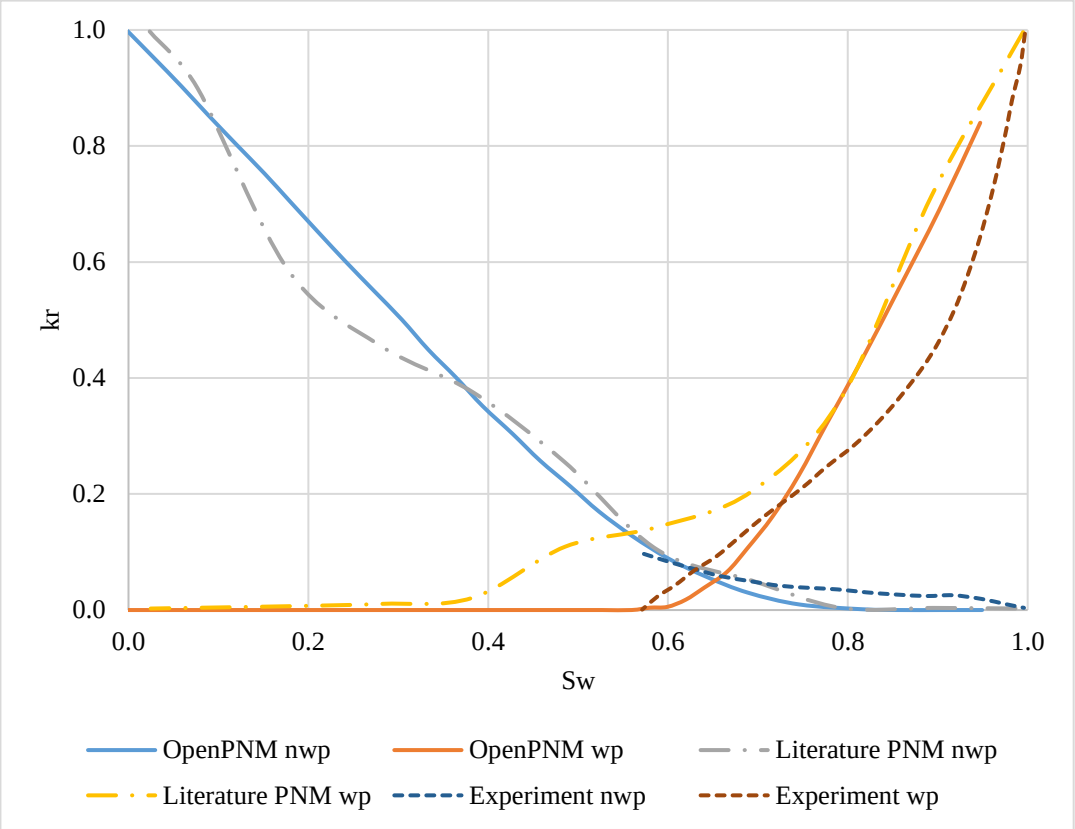

Figure 4.2 CO_2-brine relative permeability for Berea sandstone sample. Results generated in this study using OpenPNM compared to Mutailipu et al.'s (2017) PNM results and experimental results from Perrin et al. (2007).

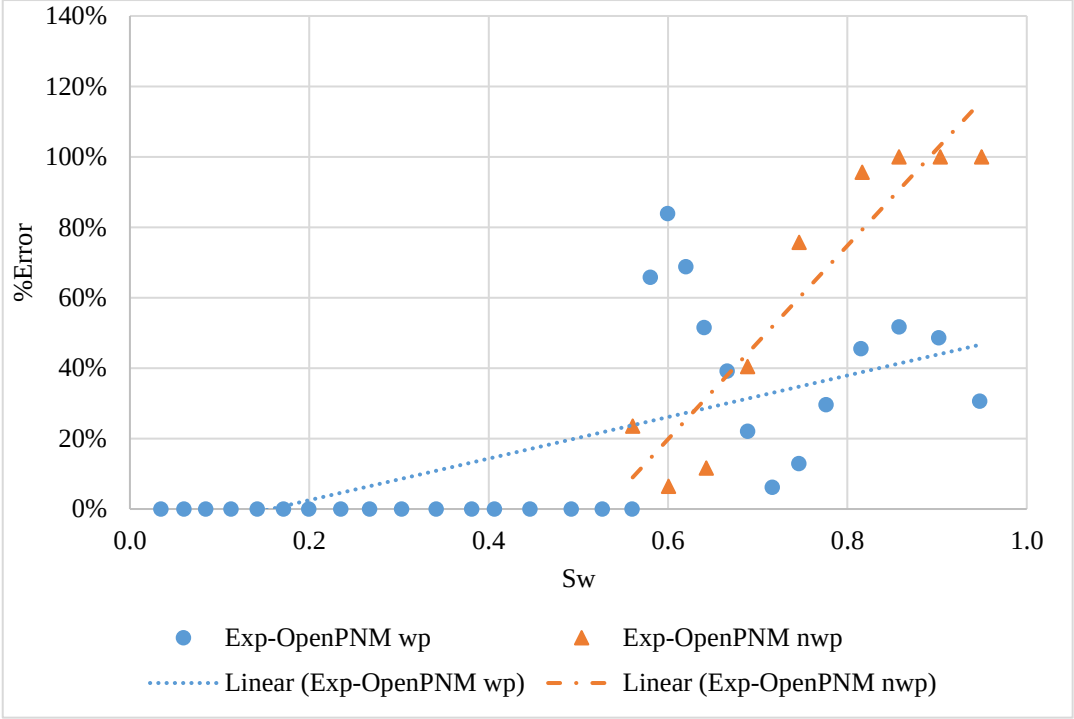

Figure 4.3 Berea Sandstone's %error trend plot for relative permeability values obtained at different saturation values for both wetting and non-wetting phases.

Mt Simon Sandstone

The relative permeability curve obtained for Mt Simon sandstone had an error of 49% compared to the literature PNM generated curve, as can be seen in Figure 4.4 and Figure 4.5. The following are the important points to note from the results:

- **Porosity:** the porosity of the network generated in OpenPNM was 21% while that of the PNM from literature is 26%, a deviation of 19%. The porosity can be concluded to be within an acceptable deviation range.
- **Wettability:** the intersection points of the curves generated through OpenPNM inclined more to the left while the other one was more toward the right. This means, at the same saturation ($S_w = 0.5$), CO_2 will flow more easily than H_2O, hence a larger k_r value. This implies that the OpenPNM generated curve indicates a CO_2-wet rock while literature data indicates a water-wet

rock. The fluid properties used in the simulation included an equal density for either fluid with CO_2 having a lower viscosity than H_2O. Since the contact angle assigned is 180°, this indicates a strongly CO_2-wet scenario, implying the results generated by OpenPNM to be correct.

- **Residual saturation:** the residual saturation of the non-wetting phase obtained using OpenPNM is similar to that from the experiment, around S_{rg}=0.2. However, the wetting phase residual saturations do not coincide.
- **Phase mobility:** both curves exhibit a flatter slope for the wetting phase indicating a lower mobility for brine and a relatively steeper slope for the non-wetting phase which has a higher mobility[12] due to its lower viscosity.

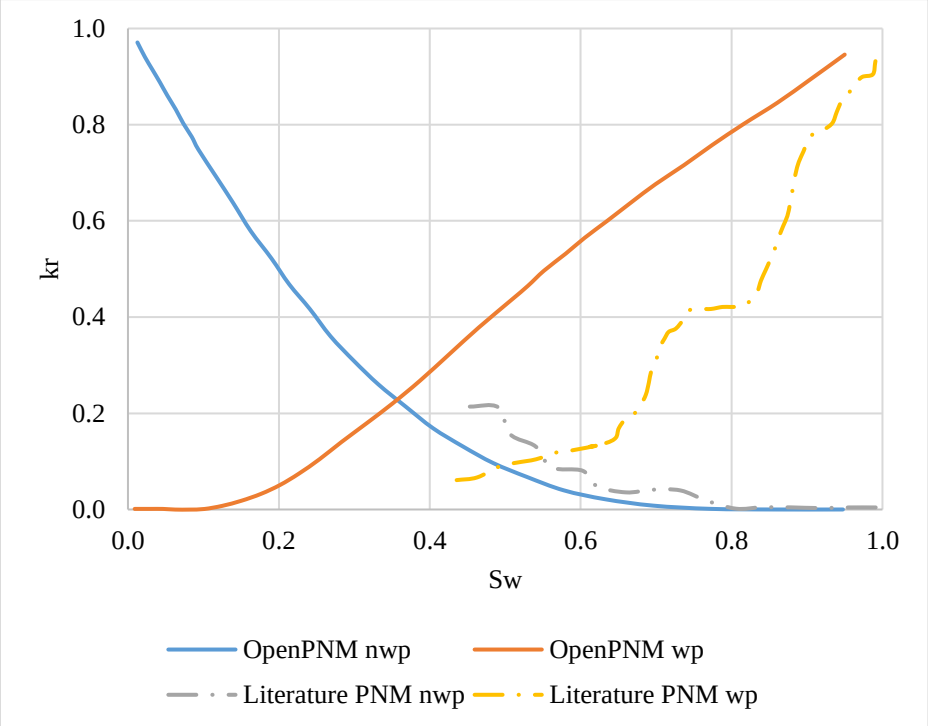

Figure 4.4 CO_2-brine relative permeability y for Mt Simon sandstone sample. Results generated in this study using OpenPNM compared to Kohanpur et al.'s (2020) PNM results.

[12] Mobility is the ratio of a phase's relative permeability to its viscosity.

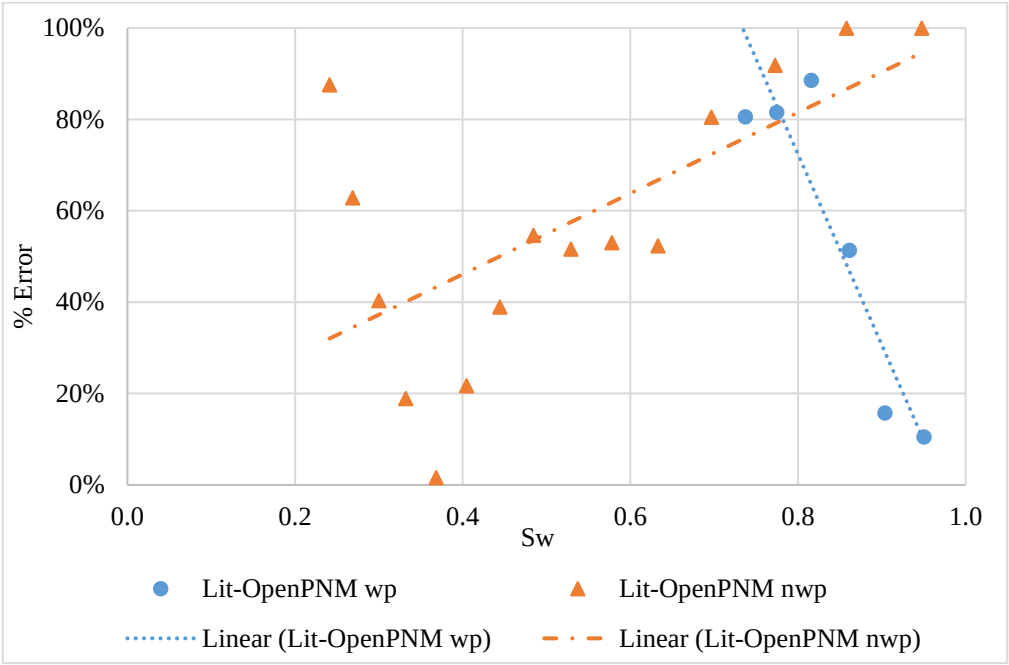

Figure 4.5 Mt Simon Sandstone's %error trend plot for relative permeability values obtained at different saturation values for both wetting and non-wetting phases.

Carbonate

The relative permeability curve obtained for the carbonate sample had an error of 26% from the literature results, as can be seen in Figure 4.6 and Figure 4.7. The following are the important points to note from the results:

- **Porosity:** the porosity of the network generated in OpenPNM was 22% and that of the compared study is 29%, a deviation of 24%.
- **Wettability:** the intersection point of the curves is inclined towards the left of the plot. This indicates that the results obtained imply a more CO_2-wet medium similar to the results of the study it is compared to. Additionally, the crossover point from OpenPNM, is very close to that from the literature PNM study.

- **Residual saturation:** the residual saturation of the wetting phase obtained using OpenPNM is similar to that from the experiment, around S_{wi}=0.28. For the non-wetting phase, it is more closely related to the given PNM results from the literature, S_{rg}=0.26. The experimental non-wetting phase results were not available in the literature.

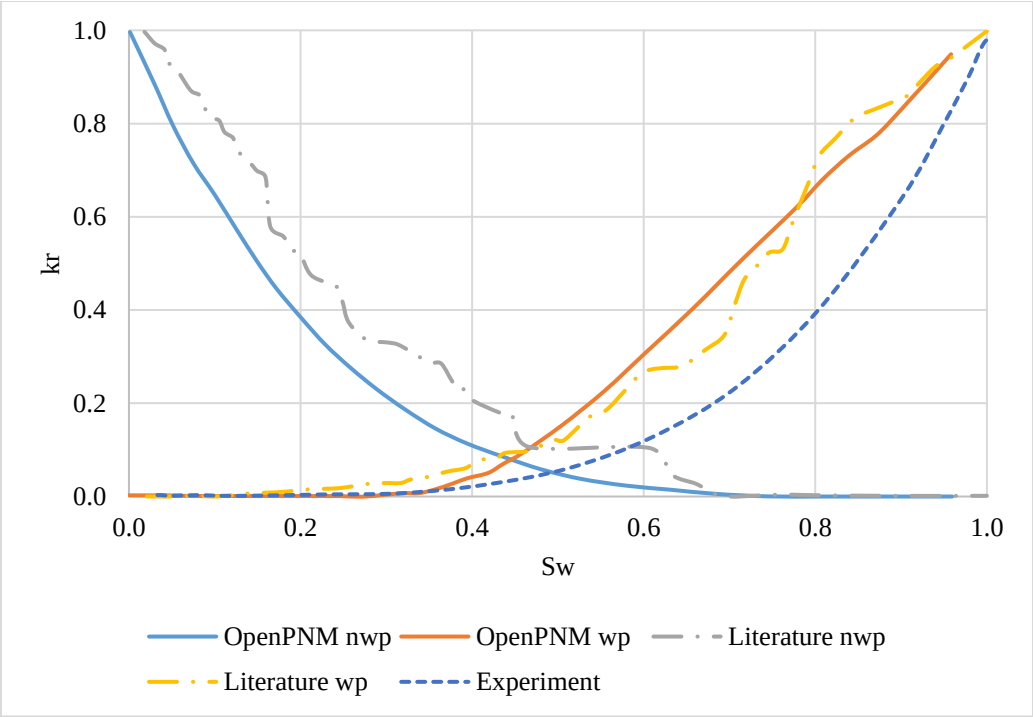

Figure 4.6 CO_2-brine relative permeability for a carbonate sample. Results generated in this study using OpenPNM are compared to Al-Kharusi & Blunt's (2008) PNM and experimental results.

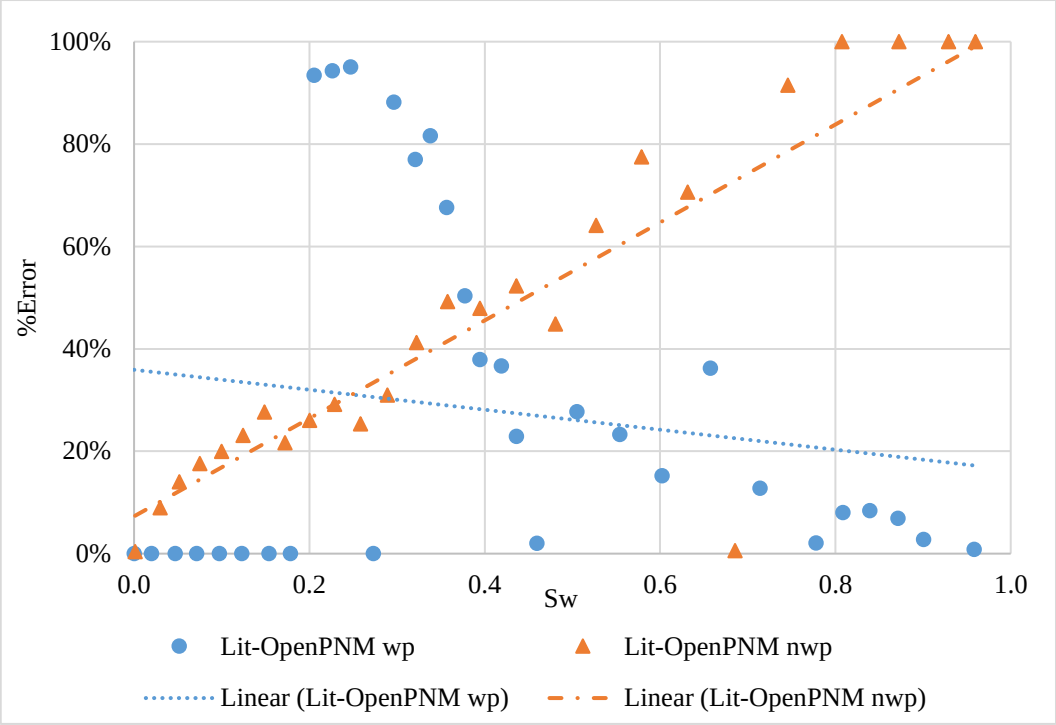

Figure 4.7 Carbonate's %error trend plot for relative permeability values obtained at different saturation values for both wetting and non-wetting phases.

4.4 General Discussion

Out of the 3 samples studied, OpenPNM generated acceptable results with an error of 18%, 49% and 26% for Berea, Mt Simon and a carbonate respectively. The most important thing to note is that Mt Simon is a sample that exhibits strong heterogeneity compared to most sandstones studied in literature like the Berea sandstone (Kohanpur et al., 2020). This strong heterogeneity is what may have caused the discrepancy in the results. Apart from limitations of OpenPNM as a tool, the following are other factors that may have caused the invalid results for Mt Simon sample:

a) Pore and throat size distributions: despite assigning the pore and throat size distributions, it is difficult to approximate the exact locations of the pores in OpenPNM while using a simple cubic lattice model. For a heterogeneous sample, it is likely to result in deviation of results.

b) Pore network geometry: the actual number of pores and throats and their connectivity is not given for this sample. These values were arbitrarily assigned and adjusted to find the best fit. However, none of the combinations generated a closer fit of the curve.

4.5 Factors Influencing Relative Permeability Behavior

To understand how different parameters that could be adjusted in OpenPNM affect the relative permeability, tests were conducted on single network. For simplicity and proven accuracy of the results, Berea sandstone network was chosen for this study. While leaving all other parameters unchanged, a single parameter was adjusted to observe the effect.

Shape: the higher the shape value, the smoother the curve. The shape determines the number of pores in either direction (x, y, z). When a smaller shape value was assigned on either direction, a larger porosity and a less smooth relative permeability curve with the same endpoint values was obtained as can be seen in Figure 4.8. We believe that the porosity increased since the same pore size distribution had to be assigned to fewer pores, making the pore sizes larger to accommodate the distribution.

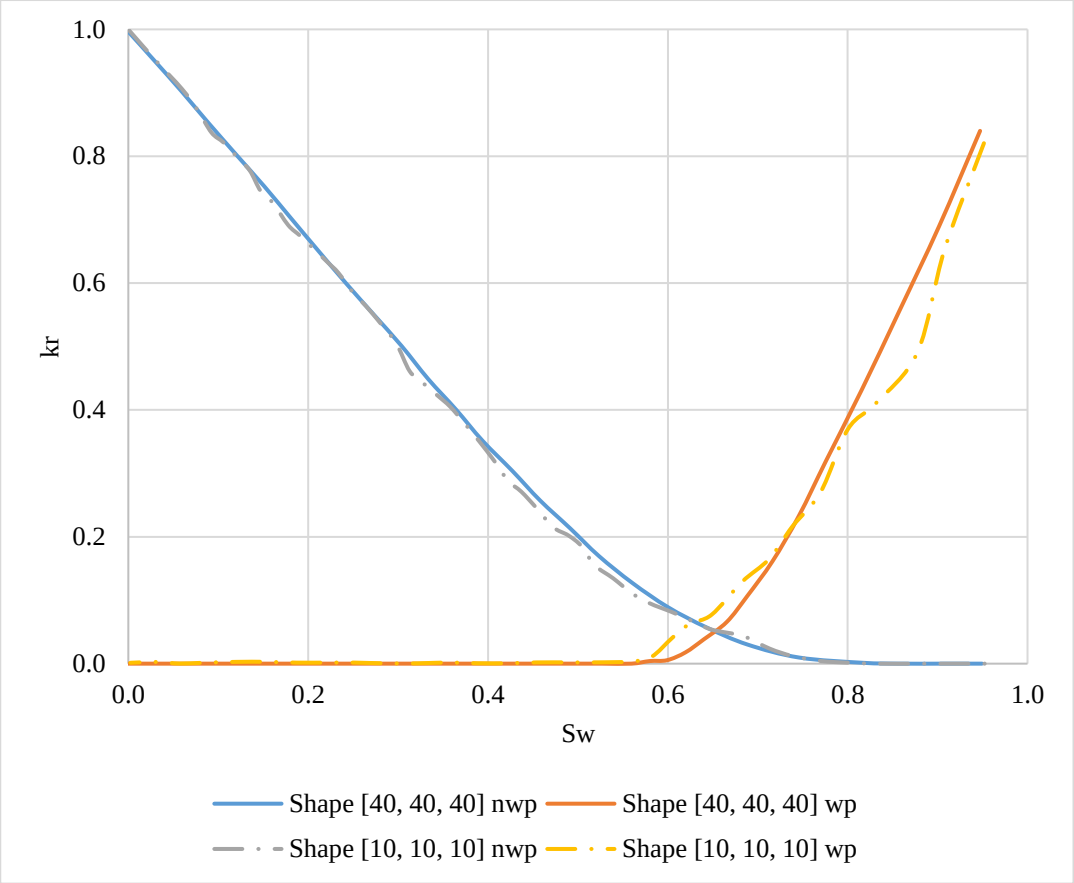

Figure 4.8. Relative permeability curves for Berea sandstone for different network shape sizes.

Spacing: this parameter defines the distance between pores. Changing the spacing of the network did not impact the relative permeability curve or the porosity value. Initially, this seemed to be a controversial finding. However, upon observing the code block that assigns the pore sizes it indicated that the changing spacing re-scales the whole network (boundaries, pores and throats). The assigned pore sizes are a function of the largest possible sphere that can be assigned to each pore position, thus the total pore volume also changes. A diameter between 20% and 70% of the largest sphere possible in each site is assigned to each sphere. The following lines describe the pore size assignment:

“

```
spheres_and_cylinders = {
    'pore.seed': {
        'model': mods.misc.random,
        'element': 'pore',
        'num_range': [0.2, 0.7],
        'seed': None,
    },
    'pore.max_size': {
        'model': mods.geometry.pore_size.largest_sphere,
        'iters': 10,
    },
    'pore.diameter': {
        'model': mods.misc.product,
        'props': ['pore.max_size', 'pore.seed'],
},
```

”

Connectivity: this parameter defines the maximum number of connections that a pore may have in a network. When the connectivity was increased, the porosity value increased and the relative permeability curve moved to the right as shown in Figure 4.9, increasing the strength of the water-wet behaviour. The porosity increased since now there are more throats connecting the pores increasing the interconnected pathways for fluid flow. The increased connectivity increases the surface area for the wetting phase to occupy the surface of the pore space. This can lead to a broader saturation range over which the wetting phase sticks to the surface making it less mobile. Hence, contributing to the observed shift in the relative permeability curve to the right.

However, when the connectivity was significantly lowered, this shifted the curve to the left as shown by ‘Connectivity 6’ in Figure 4.9,changing the wettability of the

medium. Gharbi and Blunt (2012) observed the impact of wettability and connectivity on relative permeability curves in their study and explained the reason for such an observation. Decreased connectivity causes an increased number of isolated pores which trap the wetting phase. This makes it difficult for the non-wetting phase to displace the wetting phase due to lack of enough interconnected pathways resulting into decreased mobility of the non-wetting phase.

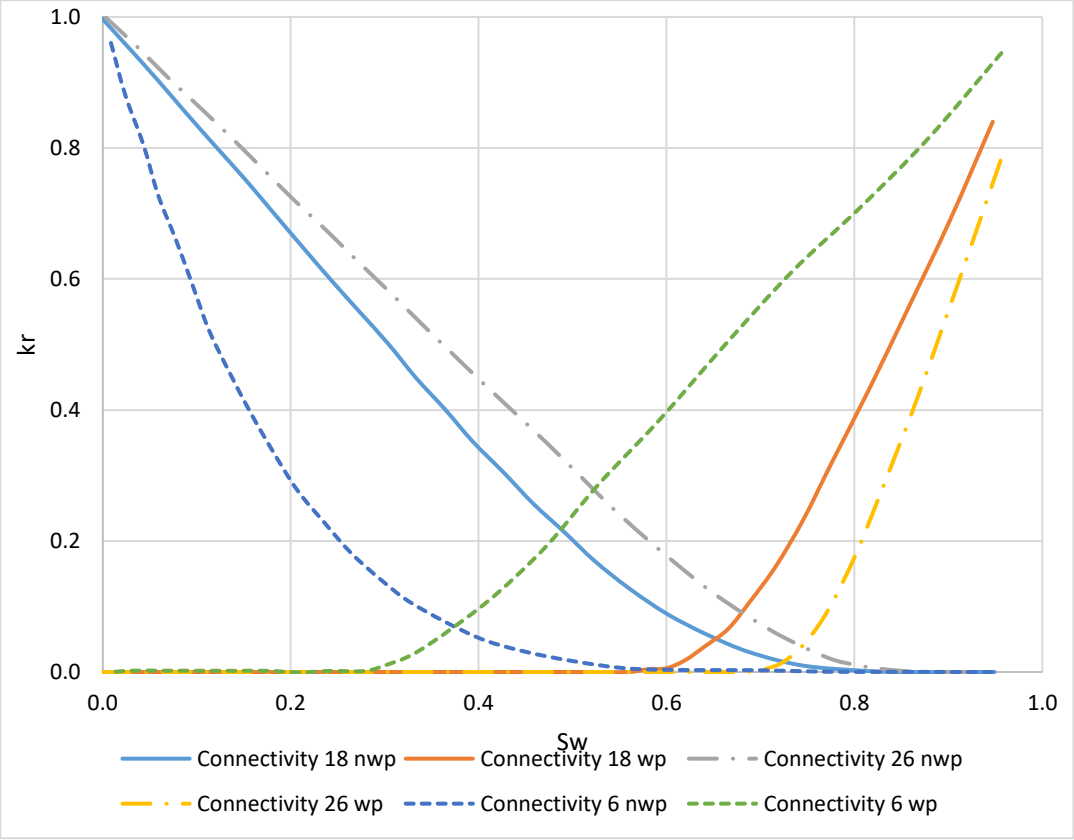

Figure 4.9 Relative permeability curves for Berea sandstone for different network connectivity (coordination number).

4.6 Corey's Relative Permeability Correlation with OpenPNM Results

Corey's correlation is used to describe the relative permeability behavior of porous media during multiphase fluid flow. In this section, the relative permeability data from OpenPNM for the three studied samples, is used to generate Corey parameters. These parameters characterize how the relative permeability of each phase changes with the saturation of that phase within the porous medium. To derive the parameters, non-linear regression was done on the relative permeability results obtained from OpenPNM. The generated trend equations were then equated with Equation (4.1) for wetting and (4.2) for non-wetting phase to derive the parameters. Table 4.2 lists the Corey parameters for both wetting (n_w) and non-wetting (n_{nw}) phase obtained for the three studied samples.

$$k_{rw} = S_w^{n_w} \tag{4.1}$$

$$k_{rnw} = (1 - S_w)^{n_{nw}} \tag{4.2}$$

Table 4.3 Corey's parameters for the wetting and non-wetting phase obtained from OpenPNM simulation results for the three samples.

Parameter	**Berea**	**Mt Simon**	**Carbonate**
$\mathbf{n_w}$	5.1	1.4	2.9
$\mathbf{n_{nw}}$	2.4	2.6	4.6

It can be observed in Figure 4.10 for Berea sandstone where the wetting phase curve indicates rapidly increasing relative permeability with the increase in saturation for a larger n_w. While for Mt Simon in Figure 4.11, there is a gradual increase in relative permeability values with increase in saturation of the wetting phase for a smaller n_w. On the other hand, Figure 4.12 for the carbonate has the largest n_{nw}, indicating a

rapid increasing relative permeability with the increase in non-wetting phase saturation.

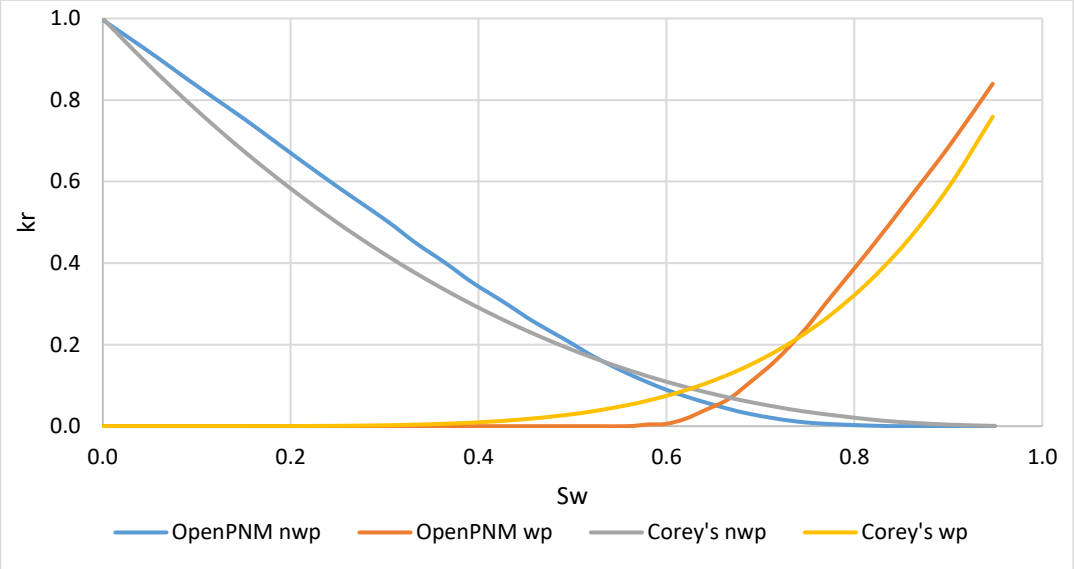

Figure 4.10 Relative permeability curves showing OpenPNM generated results and Corey's correlation predicted results for Berea sandstone.

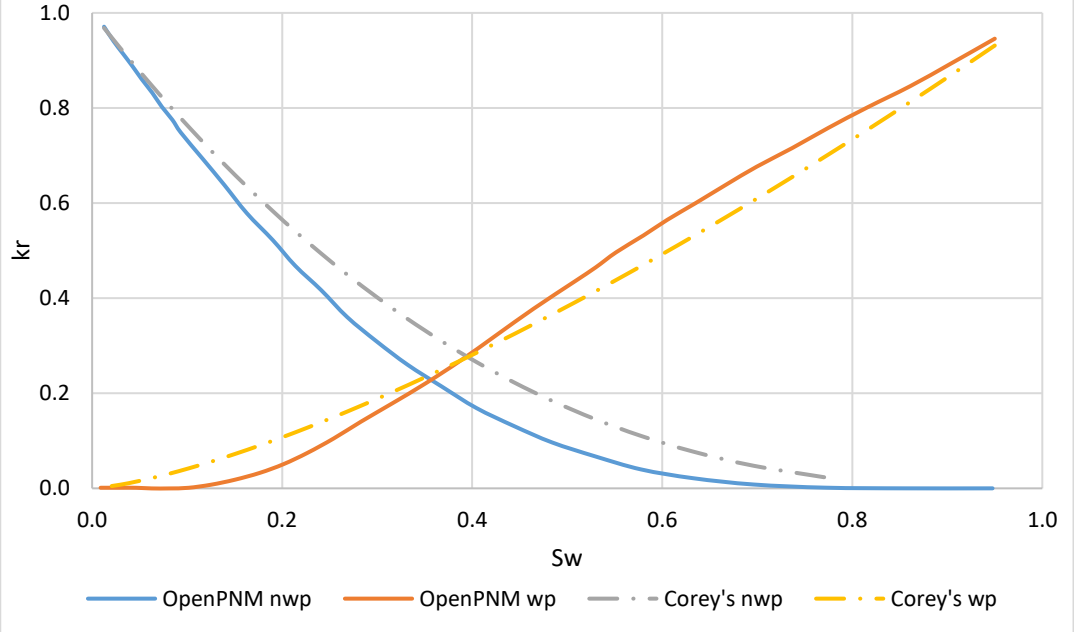

Figure 4.11 Relative permeability curves showing OpenPNM generated results and Corey's correlation predicted results for Mt Simon sandstone.

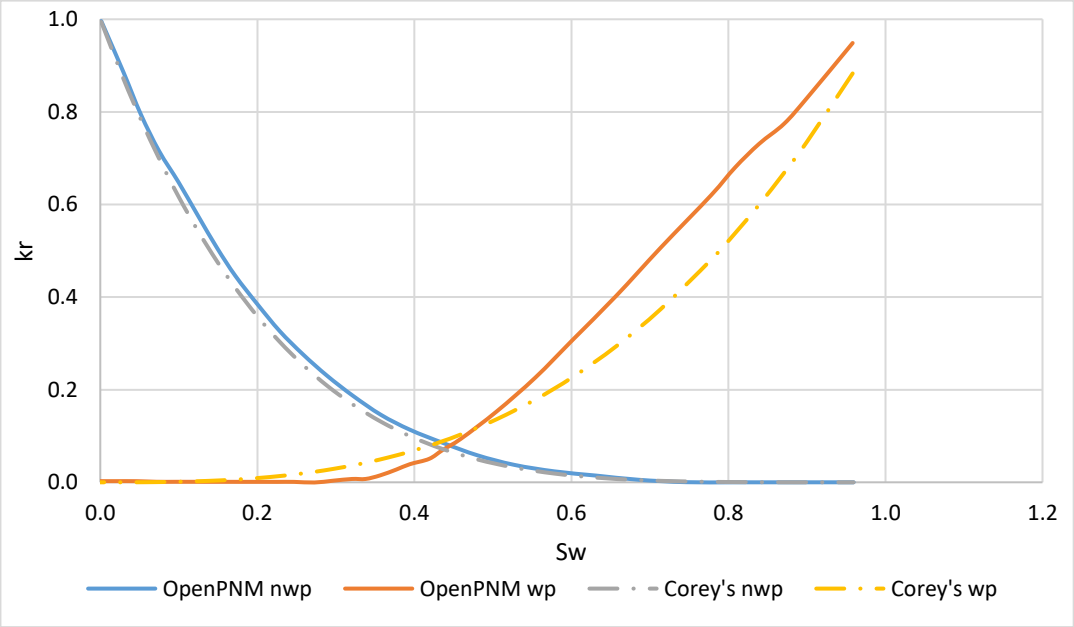

Figure 4.12 Relative permeability curves showing OpenPNM generated results and Corey's correlation predicted results for a carbonate.

CHAPTER 5

CONCLUSION

Before summarizing the results from this work, it is imperative to first emphasize on the contributions made. Relative permeability experiments can be established experimentally or using simulations. PNM, being one of the simulation methods, is a suitable option to accomodate financial and time restrictions. Several researchers have conducted PNM using algorithms created by themselves or previous researchers. There has not been any published literature found that used OpenPNM to conduct CO_2-brine relative permeability. Moreover, all the PNM studies on the subject first extracted the pore space from core sample images before importing for analysis. What was done differently in this research is that the simplified regular cubic lattice model was used as a base network. The pore and throat properties distributions existing in literature were then assigned to the model to resemble the studied sample as much as possible.

To verify the reliability of OpenPNM for predicting CO_2-brine relative permeability, obtained results were compared to experimental or other PNM results in literature. Berea sandstone results had an average error of 18% as compared to experimental results. Mt Simon sandstone had a larger deviation from the literature PNM results it was compared to, an average error of 49%. The other studied sample was a Middle Eastern originating carbonate with an average error of 26% compared to the literature PNM results. Therefore, if working with fairly homogeneous samples, the regular cubic lattice model gives better results as compared to strongly heterogenenous samples. This could be due to a poor representation of the pore space properties for strongly heterogeneous samples.

Other findings include the effect of certain network parameters to the relative permeability curve.

- When assigning the shape parameter, it is recommended to use a larger value in order to obtain smoother curves. However, one should make sure that the porosity does not exceed the expected value as the shape affects porosity. It is also important to note that, the higher the shape value, the higher the computational power required.
- Spacing did not exhibit any effect on the relative permeability curve since it is a dimensionless value. However, it could be used to adjust absolute permeability.
- Lastly, connectivity had a direct effect on porosity where increase in connectivity increased the porosity. Increase in connectivity also caused a shift of the relative permeability curve to the right making the medium more water-wet.

When modelling the network using the regular cubic lattice model, there are several limitations to the approach. The pore and throat size distributions are not location specific therefore it may differ from how they are located in the original sample. This difference highly influences the relative permeability since the flow medium structure will vary. Additionally, even though it was previously mentioned that this method does not require high computational efficiency compared to other computer simulation methods, to obtain a more detailed structure of the pore network, higher memory is required. Another limitation worth noting is the applicability of some models, particularly the geometry models. Typically, the geometrical shape of the pore and throats should affect fluid flow in the medium. However, when the different geometries were assigned, the values remained almost the same. Therefore, some assignments may still need further adjustments to properly function.

It would have been preferred to use more samples to compare the results for a precise conclusion to determine the reliability of OpenPNM. However, limitations in data accessibility constrained the number of tests to run. Additionally, it is still

recommended to first obtain a series of 2D images of pore spaces and compile them to form a 3D representation. Then the network can be extracted into a readable format using software such as PoreSpy before exporting to OpenPNM. Using OpenPNM as a pore network modelling tool allows conducting relative permeability experiments despite time or economic constraints.

REFERENCES

Acharya, T., Song, L., Duginski, E., & Goodwin, A. (2023). Evaluation of Relative Permeability Curves in Sandstone Core Flooding Using Computational Fluid Dynamics. *Processes*.

Adler, P., & Thovert, J. F. (1998). Real porous media: local geometry and macroscopic properties. *Applied Mechanics Reviews*, 537-585.

Akbarabadi, M., & Piri, M. (2013). Relative permeability hysteresis and capillary trapping characteristics of supercritical CO2/brine systems: An experimental study at reservoir conditions. *Advances in Water Resources*, 190-206.

Al-Kharusi, A. S., & Blunt, M. J. (2007). Network extraction from sandstone and carbonate pore space images. *Journal of Petroleum Science and Engineering*, 219-231.

Al-Kharusi, A. S., & Blunt, M. J. (2008). Multiphase flow predictions from carbonate pore space imagesusing extracted network models. *Water Resources Research*, 1-14.

Alley, R., Berntsen, T., Bindoff, N. L., Chen, Z., Chidthaisong, A., Friedlingstein, P., . . . M. (2007). *Climate Change 2007: The Physical Science Basis.* Paris: Intergovernmental Panel on Climate Change .

Arand, F., & Hesser, J. (2017). Accurate and efficient maximal ball algorithm for pore network extraction. *Computers & Geosciences*, 28-37.

Arigbe, O. D., Oyeneyin, M. B., Arana, I., & Ghazi, M. D. (2019). Real-time relative permeability prediction using deep learning. *Journal of Petroleum Exploration and Production Technology*, 1271-1284.

Bakhshian, S., Hosseini, S. A., & Lake, L. W. (2020). CO2-brine relative permeability and capillary pressure of Tuscaloosa sandstone: Effect of anisotropy. *Advances in Water Resources*, 1-13.

Bear, J., & Bachmat, Y. (2012). *Introduction to Modeling of Transport Phenomena in Porous Media.* Springer Science & Business Media.

Begum, A., Lempert, R. R., Ali, E., Benjaminsen, T., Bernauer, T., Cramer, W., . . . P.Wester. (2022). *IPCC Sixth Assessment Report - Impacts, Adaptation and Vulnerability.* Cambridge and New York: Cambridge University Press.

Bennion, D. B., & Bachu, S. (2008). Drainage and Imbibition Relative Permeability Relationships for Supercritical CO2/Brine and H2S/Brine Systems in Intergranular Sandstone, Carbonate, Shale, and Anhydrite Rocks. *SPE Reservoir Evaluation & Engineering*, 487-497.

Berkowitz, B., & Ewing, R. P. (1998). Percolation theory and network modeling applications in soil physics. *Surveys in Geophysics*, 23-72.

Blazek, J. (2015). *Computational Fluid Dynamics: Principles and Applications.* Elsevier.

Blunt, M. J., Bijeljic, B., Dong, H., Gharbi, O., Iglauer, S., Mostaghimi, P., . . . Pentland, C. (2013). Pore-scale imaging and modelling. *Advances in Water Resources*, 197-216.

Blunt, M. J., Jackson, M. D., Piri, M., & Valvatne, P. H. (2002). Detailed physics, predictive capabilities and macroscopic consequences for pore-network models of multiphase flow. *Advances in Water Resources*, 1069-1089.

Boccardo, G., Tosco, T., Fujisaki, A., Messina, F., Raoof, A., Aguilera, D. R., . . . Sethi, R. (2020). A review of transport of nanoparticles in porous media: from pore- to macroscale using computational methods. In B. Bonelli, F. S. Freyria, I. Rossetti, & R. Sethi, *Nanomaterials for the Detection and Removal of Wastewater Pollutants* (pp. 351-381). Elsevier.

Broadbent, S. R., & Hammersley, J. M. (1957). Percolation processes. *Mathematical Proceedings of the Cambridge Philosophical Society*, 629-641.

Brooks, R. H., & Corey, A. T. (1964). *Hydraulic Properties of Porous Media.* Fort Collins, Colorado: Hydrology Papers, Colorado State University.

Bryant, S. L., King, P. R., & Mellor, D. W. (1993). Network model evaluation of permeability and spatial correlation in a real random sphere packing. *Transport in Porous Media*, 53-70.

Burnside, N. M., & Naylor, M. (2014). Review and implications of relative permeability of CO2/brine systems and residual trapping of CO2. *International Journal of Greenhouse Gas Control*, 1-11.

Burnside, N., & Naylor, M. (2014). Review and implications of relative permeability of CO2/brine systems and residual trapping of CO2. *International Journal of Greenhouse Gas Control*, 1-11.

Burton, M., Kumar, N., & Bryant, S. L. (2009). CO2 injectivity into brine aquifers: why relative permeability matters as much as absolute permeability. *Energy Procedia*, 3091-3098.

Busch, A., & Müller, N. (2011). Determining CO2 /brine relative permeability and capillary threshold pressures for reservoir rocks and caprocks: Recommendations for development of standard laboratory protocols. *Energy Procedia*, 6053-6060.

Cannell, M. (1999). Growing trees to sequester carbon in the UK: answers to some common questions. *Forestry*, 237-247.

Carman, P. C. (1937). Fluid flow through a granular bed. *Institution of Chemical Engineers*, 32-48.

Chalbaud, C., Lombard, J. -M., Martin, F., Robin, M., Bertin, H., & Egermann, P. (2007). Two Phase Flow Properties of Brine-CO2 Systems in Carbonate Core: Influence of Wettability on Pc and kr . *SPE Reservoir Characterization and Simulation* , 1-10.

Chandler, R., Koplik, J., Lerman, K., & Willemsen, J. F. (1982). Capillary displacement and percolation in porous media. *Journal of Fluid Mechanics*, 249-267.

Chapman, R. (1983). Compaction of Sediment and Sedimentary Rocks, and its Consequences. In R. Chapman, *Petroleum Geology* (pp. 41-65). Elsevier.

Chen, X., Kianinejad, A., & DiCarlo, D. A. (2014). An Experimental Study of CO2-Brine Relative Permeability in Sandstone. *OnePetro*, 1-14.

Churcher, P., French, P., Shaw, J., & Schramm, L. (1991). Rock Properties of Berea Sandstone, Baker Dolomite, and Indiana Limestone. *OnePetro*, 431-450.

Costa, A. (2006). Permeability-porosity relationship: A reexamination of the Kozeny-Carman equation based on a fractal pore-space geometry assumption. *Geophysical Research Letters*, 1-5.

Darcy, H. (1856). *Les fontaines publiques de la ville de Dijon.* Paris: Victor Dalmont.

Doughty, C., & Pruess, K. (2004). Modeling Supercritical Carbon Dioxide Injection in Heterogeneous Porous Media. *Vadose Zone Journal*, 837-847.

Dunsmuir, J., Ferguson, S., D'Amico, K., & Stokes, J. (1991). X-Ray Microtomography: A New Tool for the Characterization of Porous Media . *OnePetro*, 423-430.

European Environment Information and Observation Network . (2022, June 22). *Global and European temperatures*. Retrieved from European Environment Agency (EEA): https://www.eea.europa.eu/ims/global-and-european-temperatures

Fatt, I. (1956). The Network Model of Porous Media. *American Institute of Mining, Metallurgical, and Petroleum Engineers*, 144-181.

Fayers, F. J., Hawes, R., & Mathews, J. (1981). Some Aspects of the Potential Application of Surfactants or CO2 as EOR Processes in North Sea Reservoirs. *Journal of Petreoleum Technology* , 1617-1627.

Flett, M., RandalIan, G., & Taggart, I. (2004). The Function of Gas-Water Relative Permeability Hysteresis in the Sequestration of Carbon Dioxide in Saline Formations. *OnePetro*, 1-11.

Flude, S. (2020). *The different trapping mechanisms that immobilise CO_2 underground*. Retrieved from Energy Post: https://energypost.eu/how-underground-ccs-works-low-leakage-risk-2/

Fu, F., Lin, L., & Xu, E. (2017). Functional pretreatments of natural raw materials . In M. Fan, & F. Fu, *Advanced High Strength Natural Fibre Composites in Construction* (pp. 87-114). Elsevier.

Gharbi, O., & Blunt, M. J. (2012). The impact of wettability and connectivity on relative permeabilityin carbonates: A pore network modeling analysis. *Water Resources Research*, 1-14.

Gil, J., & Kimmel, R. (2002). Efficient dilation, erosion, opening, and closing algorithms. *IEEE*, 1606 - 1617.

Golding, S. D., Uysal, I. T., Boreham, C. J., Kirste, D., Baublys, K. A., & Esterle, J. S. (2011). Adsorption and mineral trapping dominate CO2 storage in coal systems. *Energy Procedia*, 3131-3138.

Gong, L., Nie, L., & Xu, Y. (2020). Geometrical and Topological Analysis of Pore Space in Sandstones Based on X-ray Computed Tomography. *Energies*, 1-18.

Gostick, J. (2013). Random Pore Network Modeling of Fibrous PEMFC Gas Diffusion Media Using Voronoi and Delaunay Tessellations. *Journal of The Electrochemical Society*, 731-743.

Gostick, J., Aghighi, M., Hinebaugh, J., Tranter, T., Hoeh, M. A., Day, H., . . . Lehnert, W. (2016). OpenPNM: a pore network modeling package. *Computing in Science & Engineering*, 60-74.

Gostick, J., Aghighi, M., Hinebaugh, J., Tranter, T., Hoeh, M. A., Day, H., . . . Putz, A. (2016). OpenPNM: A Pore Network Modeling Package. *IEEE Computer Society*, 60-74.

Grimmett, G. (1999). What is Percolation? In G. Grimmett, *Percolation* (pp. 1-31). Springer, Berlin, Heidelberg.

Guo, J., Hu, Q. X., Yao, Y., Lu, Q., Yu, Y. W., & Qian, Y. (2010). A Pore Network Model Based Method for Tissue Engineering Scaffold Design. *2010 International Conference on Biomedical Engineering and Computer Science*, 1-4.

Gupta, R., & Maloney, D. R. (2016). Intercept Method—A Novel Technique To Correct Steady-State Relative Permeability Data for Capillary End Effects. *SPE Reservoir Evaluation & Engineering*, 316-330.

Hazlett, R. D. (1997). Statistical Characterization and Stochastic Modeling of Pore Networks in Relation to Fluid Flow. *Mathematical Geology*, 801-822.

Hefny, M., Qin, C., Saar, M. O., & Ebigbo, A. (2020). Synchrotron-based pore-network modeling of two-phase flow in Nubian Sandstone and implications for capillary trapping of carbon dioxide. *International Journal of Greenhouse Gas Control*.

Holt, H., Helle, K., & Brown, J. (2012). *CCS CO2 RISK MANAGEMENT – NEW INDUSTRY GUIDANCE*. Det Norske Veritas Ltd.

Holt, R. M., Fjaer, E., Torsaeter, O., & Bakke, S. (1996). Petrophysical laboratory measurements for basin and reservoir evaluation . *Marine and Petroleum Geology*, 383-391.

Ioannidis, M. A., & Chatzis, I. (1993). Network modelling of pore structure and transport properties of porous media. *Chemical Engineering Science*, 951-972.

IPCC. (2005). *IPCC Special Report on Carbon Dioxide Capture and Storage.* Cambridge: Cambridge University Press.

Jacob, B., & Yehuda, B. (1990). *Introduction to modeling of transport phenomena in porous media.* United States: Kluwer Academic Publishers.

Jiang, Z., Dijke, M. I., Sorbie, K. S., & Couples, G. D. (2013). Representation of multiscale heterogeneity via multiscale pore networks . *Water Resources Research*, 5437–5449.

Jivkov, A. P., Hollis, C., Etiese, F., McDonald, S. A., & Withers, P. J. (2013). A novel architecture for pore network modelling with applications to permeability of porous media. *Journal of Hydrology*, 246-258.

Kamann, P. J., Ritzi, R. W., Dominic, D. F., & Conrad, C. M. (2007). Porosity and Permeability in Sediment Mixtures. *Groundwater*, 429-438.

Kantzas, A., Bryan, J., & Taheri, S. (n.d.). *Fundamentals of Fluid Flow in Porous Media.* PERM Inc.

Kashkooli, S. B., Gandomkar, A., Riazi, M., & Tavallali, M. S. (2022). The investigation of gas trapping and relative permeability alteration during optimization of CO2-EOR and sequestration. *International Journal of Greenhouse Gas Control*.

Khaz'ali, A. R., Emamjomeh, A., & Andayesh, M. (2011). An Accuracy Comparison Between Artificial Neural Network and Some Conventional Empirical Relationships in Estimation of Relative Permeability. *Petroleum Science and Technology* , 1603-1614.

Kohanpur, A. H., Rahromostaqim, M., Valocchi, A. J., & Sahimi, M. (2020). Two-phase flow of CO2-brine in a heterogeneous sandstone: Characterization of

the rock and comparison of the lattice-Boltzmann, pore-network, and direct numerical simulation methods. *Advances in Water Resources*.

Kopp, A., Class, H., & Helmig, R. (2009). Investigations on CO2 storage capacity in saline aquifers: Part 1. Dimensional analysis of flow processes and reservoir characteristics. *International Journal of Greenhouse Gas Control*, 263-276.

Leitner, D., Bodner, G., & Raoof, A. (2013). Coupling root architecture and pore network modeling - an attempt towards better understanding root-soil interactions. *EGU General Assembly 2013*.

Leuitz, P. E. (2002). Statistical Modeling of Pore Networks. In F. Schüth, K. S. Sing, & J. Weitkamp, *Handbook of Porous Solids* (pp. 35-80). WILEY-VCH Verlag GmbH.

Li, W., Mu, L., Zhao, L., Li, J., Wang, S., Fan, Z., . . . Sun, M. (2020). Pore-throat structure characteristics and its impact on the porosity and permeability relationship of Carboniferous carbonate reservoirs in eastern edge of Pre-Caspian Basin. *Petroleum Exploration and Development*, 1027-1041.

Liu, H., Ma, C., & Zhu, C. (2022). X-ray Micro CT Based Characterization of Pore-Throat Network for Marine Carbonates from South China Sea. *Applied Science*.

Lopez, O., Idowu, N., Mock, A., Rueslåtten, H., Boassen, T., Leary, S., & Ringrose, P. (2011). Pore-scale modelling of CO2 -brine flow properties at In Salah, Algeria. *Energy Procedia*, 3762-3769.

Manwart, C., Torquato, S., & Hilfer, R. (2000). Stochastic reconstruction of sandstones. *Physical Review E*, 893-899.

Martínez-Mendoza, E. G., Díaz-Viera, M. A., Coronado, M., & Mendoza-Rosas, A. T. (2019). Capillary pressure and relative permeability estimation for low

salinity waterflooding processes using pore network models. *Journal of Petroleum Science and Engineering*, 1-18.

Martins, P. H., & Gonzalez, M. (2022). A Process-Based Pore Network Model Construction for Granular Packings Under Large Plastic Deformations. *Transport in Porous Media* , 45-72.

McPhee, C., Reed, J., & Zubizarreta, I. (2015). *Core Analysis: A Best Practice Guide.* Elsevier.

Mehmani, A., & Prodanovic, M. (2014). The effect of microporosity on transport properties in porous media. *Advances in Water Resources*, 104-119.

Miaomiao, L., Benbiao, S., Changbing, T., & Xianyu, M. (2022). Relationship between pore throat and permeability of porous carbonate reservoir in the Middle East. *Arabian Journal of Geosciences*, 1-7.

Miller, C. T., Christakos, G., Imhoff, P. T., McBride, J. F., Pedit, J. A., & Trangenstein, J. A. (1998). Multiphase flow and transport modeling in heterogeneous porous media: challenges and approaches. *Advances in Water Resources*, 77-120.

Milliken, K. L. (2003). Late Diagenesis and Mass Transfer in Sandstone–Shale Sequences. In *Treatise on Geochemistry* (pp. 159-190). Elsevier.

Mohammadi, A., Rasaei, M. R., Mashayekhizadeh, V., & Nakhaee, A. (2022). Pore-network modelling of combined molecular diffusion and gravity drainage mechanisms in a porous matrix block: The competitive role of driving forces. *The Canadian Journal of Chemical Engineering*, 2341-3008.

Moodie, N., Ampomah, W., Jia, W., Heath, J., & McPherson, B. (2019). Assignment and calibration of relative permeability by hydrostratigraphic units for multiphase flow analysis, case study: CO2-EOR operations at the Farnsworth Unit, Texas. *International Journal of Greenhouse Gas Control*, 103-114.

Moodie, N., Pan, F., Jia, W., & McPherson, B. (2017). Impacts of relative permeabilityformulation on forecasts of CO2phase behavior, phase distribution,and trapping mechanisms in ageologic carbon storage reservoir. *Greenhouse Gases: Science and Technology*, 215-394.

Moore, J., Holcomb, P., Crandall, D., King, S., Choi, J.-H., Brown, S., & Workman, S. (2021). Rapid determination of supercritical CO2 and brine relative permeability using an unsteady-state flow method. *Advances in Water Resources*, 1-11.

Mufti, S., & Das, A. (2023). Pore network modeling approach for simulating soil water retention curve under different stress conditions. *8th International Conference on Unsaturated Soils (UNSAT 2023)*, 1-6.

Mutailipu, M., Liu, Y., Wu, B., Song, Y., Wang, D., & Ai, L. (2017). Gas-Water Two Phase Flow Simulation Based on Pore Network Model for Reservoir Rocks. *Energy Procedia*, 3214-3219.

Okabe, H., & Blunt, M. (2004). Prediction of permeability for porous media reconstructed using multiple-point statistics. *Physical Review E*.

OpenPNM. (2022). *Geometry*. Retrieved from OpenPNM: https://openpnm.org/modules/generated/openpnm.models.geometry.html

OpenPNM. (2023). *Cubic*. Retrieved from OpenPNM: https://openpnm.org/modules/generated/openpnm.network.Cubic.html#openpnm.network.Cubic

Øren, P.-E., & Bakke, S. (2002). Process Based Reconstruction of Sandstones and Prediction of Transport Properties. *Transport in Porous Media*, 311-343.

Øren, P.-E., & Bakke, S. (2003). Reconstruction of Berea sandstone and pore-scale modelling of wettability effects. *Journal of Petroleum Science and Engineering*, 177-199.

Øren, P.-E., Bakke, S., & Arntzen, O. J. (1996). Extending Predictive Capabilities to Network Models. *OnePetro*, 324-336.

Ovejas, V. J., & Cuadras, A. (2018). Impedance Characterization of an LCO-NMC/Graphite Cell: Ohmic Conduction, SEI Transport and Charge-Transfer Phenomenon. *Batteries*, 1-22.

Ozden, A., Alaefour, I. E., Shahgaldi, S., Li, X., Colpan, C. O., & Hamdullahpur, F. (2018). Gas Diffusion Layers for PEM Fuel Cells. *Exergetic, Energetic and Environmental Dimensions*, 695-727.

Patzek, T. W. (2001). Verification of a Complete Pore Network Simulator of Drainage and Imbibition. *SPE Journal*, 144-156.

Percolation and Clustering. (2002). In S. Torquato, *Random Heterogeneous Materials: Microstructure and Macroscopic Properties* (pp. 211-231). Springer-Verlag.

Perrin, J.-C., Krausea, M., Kuoa, C.-W., Miljkovic, L., Charoba, E., & Benson, S. M. (2009). Core-scale experimental study of relative permeability properties of CO2 and brine in reservoir rocks. *Energy Procedia*, 3515-3522.

PetroWiki. (2016). *Relative Permeability Models*. Retrieved from PetroWiki: https://petrowiki.spe.org/Relative_permeability_models

Potter, P. E., Maynard, J. B., Jackson, D., & Dereamer, J. (1984). *Lithologic and environmental atlas of Berea Sandstone (Mississippian) in the Appalachian Basin.* Final Report Cincinnati Univ., OH. Lab. of Sedimentology.

Ramstad, T., Berg, C. F., & Thompson, K. (2019). Pore-Scale Simulations of Single- and Two-Phase Flow in Porous Media: Approaches and Applications. *Transport in Porous Media*, 77-104.

Raoof, A., & Hassanizadeh, S. M. (2010). A New Method for Generating Pore-Network Models of Porous Media. *Transport in Porous Media* , 391- 407.

Rapp, B. E. (2017). Fluids. In *Microfluidics: Modeling, Mechanics and Mathematics* (pp. 243-263). Elsevier.

Richardson, J. G. (1957). The Calculation of Waterflood Recovery from Steady-State Relative Permeability Data. *J Pet Technol*, 64-66.

Ritchie, H., Roser, M., & Rosado, P. (2020). *CO_2 and Greenhouse Gas Emissions*. Retrieved from Our World in Data: https://ourworldindata.org/emissions-by-sector

Rosenbauer, R., & Thomas, B. (2010). Carbon dioxide (CO2) sequestration in deep saline aquifers and formations. In *Developments and Innovation in Carbon Dioxide (CO2) Capture and Storage Technology* (pp. 57-103). Woodhead Publishing .

Sahimi, M. (2011). *Flow and Transport in Porous Media and Fractured Rock: From Classical Methods to Modern Approaches.* John Wiley & Sons.

Saxena, N., Mavko, G., Hofmann, R., & Srisutthiyakorn, N. (2017). Estimating permeability from thin sections without reconstruction: Digital rock study of 3D properties from 2D images. *Computers & Geosciences*, 79-99.

Sedaghatinasab, R., Kord, S., Moghadasi, J., & Soleymanzadeh, A. (2021). Relative Permeability Hysteresis and Capillary Trapping during CO2 EOR and Sequestration. *International Journal of Greenhouse Gas Control*.

Thacker, B., Doebling, S., Hemez, F., Anderson, M., Pepin, J., & Rodriguez, E. (2004). *Concepts of Model Verification and Validation.* Los Alamos, USA: Los Alamos National Laboratory.

Trombley, C. I., & Ekiel-Jeżewska, M. L. (2019). Basic Concepts of Stokes Flows. In F. Toschi, & M. Sega, *Flowing Matter* (pp. 35-50). Springer, Cham.

UNICEF. (2022). *Devastating floods in Pakistan*. Retrieved from UNICEF: https://www.unicef.org/emergencies/devastating-floods-pakistan-2022

United Nations. (2016). *The Paris Agreement*. Retrieved from United Nations Climate Action: https://www.un.org/en/climatechange/paris-agreement

United Nations. (2017). *Key Aspects of the Paris Agreement*. Retrieved from United Nations Climate Change: https://unfccc.int/most-requested/key-aspects-of-the-paris-agreement#:~:text=The%20Paris%20Agreement's%20central%20aim,further%20to%201.5%20degrees%20Celsius.

Varloteaux, C., Békri, S., & Adler, P. M. (2013). Pore network modelling to determine the transport properties in presence of a reactive fluid: From pore to reservoir scale. *Advances in Water Resources*, 87-100.

Vogel, H.-J., & Roth, K. (2001). Quantitative morphology and network representation of soil pore structure. *Advances in Water Resources* , 233-242.

Wang, J., Zhao, J., Zhang, Y., Wang, D., Li, Y., & Song, Y. (2016). Analysis of the effect of particle size on permeability in hydrate-bearing porous media using pore network models combined with CT. *Fuel*, 34-40.

Wang, L., He, Y., Chen, H., Z. M., & Wang, Z. (2019). Experimental investigation of the live oil-water relative permeability and displacement efficiency on Kingfisher waxy oil reservoir. *Journal of Petroleum Science and Engineering*, 1029-1043.

Wegener, D. C., & Harpole, K. J. (1996). Determination of Relative Permeability and Trapped Gas Saturation for Predictions of WAG Performance in the South Cowden C02 Flood. *OnePetro*, 273-285.

Wilkinson, D., & Willemsen, J. F. (1983). Invasion percolation: a new form of percolation theory. *Journal of Physics A: Mathematical and General*, 3365-3376.

Wu, Y., Tahmasebi, P., Yu, H., Lin, C., Wu, H., & Dong, C. (2019). Pore-Scale 3D Dynamic Modeling and Characterization of Shale Samples: Considering the

Effects of Thermal Maturation. *Journal of Geophysical Research: Solid Earth*, 1-22.

WWF Australia. (2020). *Emergency response to the Australian bushfires*. Retrieved from WWF: https://www.wwf.org.au/what-we-do/bushfires

Wypych, G. (2017). Analytical Techniques Useful in Foaming. In G. Wypych, *Handbook of Foaming and Blowing Agents* (pp. 219-225). ChemTec Publishing.

Xiong, Q., Baychev, T. G., & Jivkov, A. P. (2016). Review of pore network modelling of porous media: Experimental characterisations, network constructions and applications to reactive transport. *Journal of Contaminant Hydrology*, 101-117.

Yang, F., Bai, B., Tang, D., Shari, D.-N., & David, W. (2010). Characteristics of CO2 sequestration in saline aquifers. *Petroleum Science*, 83-92.

Yeong, C. L., & Torquato, S. (1998). Reconstructing random media. *Physical Review E*, 495-506.

Yuan, C., Chareyre, B., & Darve, F. (2015). A Pore-Scale Approach of Two-Phase Flow in Granular Porous Media. *Particles*, 957-968.

Zhang, D., & Song, J. (2014). Mechanisms for geological carbon sequestration. *Procedia IUTAM*, 319-327.

Zhang, P., Lee, Y. I., & Zhang, J. (2019). A review of high-resolution X-ray computed tomography applied to petroleum geology and a case study. *Micron*, 1-10.

Zhao, J., Qin, F., Derome, D., Kang, Q., & Carmeliet, J. (2020). Improved pore network models to simulate single-phase flow in porous media by coupling with lattice Boltzmann method. *Advances in Water Resources*.

Zhmakin, A. I. (2021). Heat Conduction Beyond the Fourier Law. *Technical Physics volume*, 1-22.

APPENDICES

A. The Code for Mt Simon

```
# In[1]:

import numpy as np
import openpnm as op
import matplotlib.pyplot as plt
import pandas as pd
from scipy.stats import gamma  #gamma distribution resembles the requirement
op.visualization.set_mpl_style()
np.random.seed(10)
# get_ipython().run_line_magic('matplotlib', 'inline')
np.set_printoptions(precision=5)


# In[2]:

#Creating Network
pn = op.network.Cubic(shape=[40, 40, 40], spacing=1e-5, connectivity=26)
#spacing unit in metres
pn.add_model_collection(op.models.collections.geometry.spheres_and_cylinders)
pn.regenerate_models()
print(pn)
fig, ax = plt.subplots()
op.visualization.plot_coordinates(pn, c='lightgrey', markersize=50, ax=ax)
op.visualization.plot_connections(pn, ax=ax);


# In[3]:

#adjusting the pore size distribution
N = pn.Np # per pn.pore.diameter count
```

```
bin_centers = [1.42E-06, 2.34E-06, 3.26E-06, 4.44E-06, 5.57E-06, 6.50E-06, 7.44E-06, 8.56E-06, 9.44E-06, 1.06E-05, 1.15E-05, 1.27E-05, 1.37E-05, 1.47E-05, 1.57E-05, 1.68E-05, 1.78E-05, 1.88E-05, 1.98E-05, 2.08E-05, 2.18E-05, 2.28E-05, 2.38E-05, 2.49E-05, 2.59E-05, 2.71E-05, 2.79E-05, 2.90E-05, 3.01E-05, 3.11E-05, 3.20E-05, 3.31E-05, 3.42E-05, 3.52E-05, 3.61E-05, 3.72E-05, 3.81E-05, 3.92E-05, 4.02E-05, 4.13E-05, 4.23E-05, 4.33E-05, 4.43E-05, 4.54E-05, 4.64E-05, 4.74E-05, 4.84E-05, 4.94E-05, 5.05E-05, 5.16E-05]  # In metres
bin_height = [0.0166, 0.0362, 0.0476, 0.0572, 0.0468, 0.0469, 0.0370, 0.0331, 0.0312, 0.0377, 0.0333, 0.0409, 0.0372, 0.0293, 0.0365, 0.0316, 0.0358, 0.0366, 0.0273, 0.0304, 0.0287, 0.0229, 0.0206, 0.0174, 0.0197, 0.0181, 0.0155, 0.0123, 0.0097, 0.0102, 0.0129, 0.0097, 0.0081, 0.0083, 0.0045, 0.0045, 0.0045, 0.0026, 0.0026, 0.0015, 0.0032, 0.0018, 0.0018, 0.0007, 0.0011, 0.0004, 0.0021, 0.0007, 0.0003, 0.0008]  # Normalized to sum to 1.0
r = np.zeros(N)
i = 0
while i < N:
    mybin = np.random.randint(len(bin_centers))
    if np.random.rand() < bin_height[mybin]:
        r[i] = bin_centers[mybin]
        i += 1
plt.figure(figsize=[8,8])
plt.hist(r, edgecolor='k', label='Pore Size Distribution')

# In[4]:

#assign new pore sizes to network
pn['pore.diameter'] = r
```

```
# In[5]:
#adjusting the throat size distribution
T = pn.Nt  # per pn.throat.diameter count
bin_centers = [3.96E-07, 1.22E-06, 2.09E-06, 2.91E-06, 3.84E-06, 4.70E-06, 5.51E-06, 6.30E-06, 7.23E-06, 8.04E-06, 8.84E-06, 9.64E-06, 1.05E-05, 1.14E-05, 1.23E-05, 1.32E-05, 1.39E-05, 1.49E-05, 1.57E-05, 1.65E-05, 1.73E-05, 1.81E-05, 1.90E-05, 2.00E-05, 2.08E-05, 2.16E-05, 2.24E-05, 2.32E-05, 2.42E-05, 2.49E-05, 2.58E-05, 2.67E-05, 2.75E-05, 2.83E-05, 2.93E-05] # In metres
bin_height = [0.0395, 0.0675, 0.0772, 0.0950, 0.0938, 0.0851, 0.0871, 0.0719, 0.0698, 0.0696, 0.0648, 0.0587, 0.0443, 0.0434, 0.0367, 0.0265, 0.0280, 0.0219, 0.0167, 0.0141, 0.0110, 0.0081, 0.0067, 0.0080, 0.0060, 0.0056, 0.0013, 0.0017, 0.0010, 0.0019, 0.0010, 0.0008, 0.0016, 0.0015, 0.0002]  # Normalized to sum to 1.0
t = np.zeros(T)
i = 0
while i < T:
    mybin = np.random.randint(len(bin_centers))
    if np.random.rand() < bin_height[mybin]:
        t[i] = bin_centers[mybin]
        i += 1
plt.figure(figsize=[8,8])
plt.hist(t, edgecolor='k', label='Throat Size Distribution')

# In[6]:

#assign new throat sizes to network
pn['throat.diameter'] = t
pn.regenerate_models()
```

In[7]:

```
#generating pore data sheet
pore_data_sheet = pd.DataFrame({k: pn[k] for k in pn.props(element='pore') if pn[k].ndim == 1})
pore_data_sheet
```

In[8]:

```
# Using DataFrame.mean() method to get column average
z_org = pore_data_sheet["pore.coordination_number"].mean()
print(z_org)
```

In[9]:

```
# Generating an array marking the throats to be removed, as true/false in a list:
dropB = op.topotools.reduce_coordination(network=pn, z=5)
# Full list of throats
ithroatALL =np.arange(0, pn.Nt)
# Making an array of pore indices:
marr = np.ma.MaskedArray(ithroatALL, mask=~dropB)
ithroatDrop = marr.compressed()
#Trimming random pores in the network
op.topotools.trim(network=pn, throats=ithroatDrop)
pn.regenerate_models()
```

In[10]:

```
#Assigning the new mean coordination number
data_sheet_new = pd.DataFrame({k: pn[k] for k in pn.props(element='pore') if pn[k].ndim == 1})
z_new = data_sheet_new["pore.coordination_number"].mean()
print(z_new)
```

```
# In[11]:

#for checking the network health
pn.add_model(propname='pore.cluster_number',
             model=op.models.network.cluster_number)
pn.add_model(propname='pore.cluster_size',
             model=op.models.network.cluster_size)
health = op.utils.check_network_health(pn)

# In[12]:

#generating the new data sheet
data_sheet_new

# In[13]:

#Creating Wetting phase (brine)
brine = op.phase.Phase(network=pn)
brine['pore.density'] = 1100  # kg/m3
brine['pore.viscosity'] = 0.0011  # Pa.s
print(brine)
print (brine.models)
brine.regenerate_models()

# In[14]:

#Creating Non-wetting phase (CO2)
co2 = op.phase.Phase(network=pn)
co2['pore.density'] = 1100  # kg/m3
co2['pore.viscosity'] = 0.00011  # Pa.s
co2['throat.viscosity'] = 0.00011  # Pa.s
co2['pore.contact_angle'] = 180
co2['throat.contact_angle'] = 180
```

```
co2['throat.surface_tension'] = 30.0  # mN/m #for calculating Pc using contact angle
and throat diameter
print (co2)
print (co2.models)
co2.regenerate_models()

# In[15]:

f= op.models.physics.capillary_pressure.washburn
co2.add_model                    (propname='throat.entry_pressure',model=f,
surface_tension='throat.surface_tension',
            contact_angle='throat.contact_angle', diameter='throat.diameter')

# In[16]:

# Set the viscosity values for each throat
pn['throat.viscosity'] = 0.00011 #Pa.s  # Assign a single value to all throats
# Create a custom model function for the Hagen-Poiseuille conductance
def hagen_poiseuille(target, throat_diameter='throat.diameter',
                  throat_length='throat.length', throat_viscosity='throat.viscosity',
                  size_factors=None):
    diameter = target[throat_diameter]
    length = target[throat_length]
    viscosity = target[throat_viscosity]
    conductance = (np.pi / 128) * (diameter ** 4) / (length * viscosity)
    if size_factors is not None:
        conductance *= size_factors
    return conductance
# Add the Hagen-Poiseuille model to the network
pn.add_model(propname='throat.hydraulic_conductance', model=hagen_poiseuille)
pn.regenerate_models()
```

```
# In[17]:

#Applying invasion percolation
ip = op.algorithms.InvasionPercolation(network=pn, phase=co2)
Finlets_init = pn.pores('left')
Finlets=([Finlets_init[x] for x in range(0, len(Finlets_init), 2)])
ip.set_inlet_BC(pores=Finlets)
ip.run()


# In[18]:

#Occupancy and permeability functions
def sat_occ_update(network, nwp, wp, ip, i):
    r"""
        Calculates the saturation of each phase using the invasion
        sequence from either invasion percolation.
        Parameters
        ----------
        network: network
        nwp : phase
            non-wetting phase
        wp : phase
            wetting phase
        ip : IP
            invasion percolation (ran before calling this function)
        i: int
            The invasion_sequence limit for masking pores/throats that
            have already been invaded within this limit range. The
            saturation is found by adding the volume of pores and thorats
            that meet this sequence limit divided by the bulk volume.
    """
    pore_mask = ip['pore.invasion_sequence'] < i
```

```
    throat_mask = ip['throat.invasion_sequence'] < i
    sat_p = np.sum(network['pore.volume'][pore_mask])
    sat_t = np.sum(network['throat.volume'][throat_mask])
    sat1 = sat_p + sat_t
    bulk = network['pore.volume'].sum() + network['throat.volume'].sum()
    sat = sat1/bulk
    nwp['pore.occupancy'] = pore_mask
    nwp['throat.occupancy'] = throat_mask
    wp['throat.occupancy'] = 1-throat_mask
    wp['pore.occupancy'] = 1-pore_mask
    return sat

# In[19]:

#Function to calculate rate
def Rate_calc(network, phase, inlet, outlet, conductance):
    phase.regenerate_models()
    St_p = op.algorithms.StokesFlow(network=network, phase=phase)
    St_p.settings._update({'conductance' : conductance})
    St_p.set_value_BC(pores=inlet, values=600000) #Set the inlet pressure
    St_p.set_value_BC(pores=outlet, values=500000) #Set the outlet pressure
    St_p.run()
    val = np.abs(St_p.rate(pores=inlet, mode='group'))
    return val

# In[20]:

#Defining inlet and outlet pores
flow_in = pn.pores('left')
flow_out = pn.pores('right')
```

In[21]:

```
#Defining multiphase conductance
model_mp_cond = op.models.physics.multiphase.conduit_conductance
brine.add_model(model=model_mp_cond,
propname='throat.conduit_hydraulic_conductance',
        throat_conductance='throat.hydraulic_conductance',        mode='medium',
regen_mode='deferred')
co2.add_model(model=model_mp_cond,
propname='throat.conduit_hydraulic_conductance',
        throat_conductance='throat.hydraulic_conductance',        mode='medium',
regen_mode='deferred')
brine.regenerate_models()
co2.regenerate_models()
```

In[22]:

```
#Calculating relative permeability
Snwp_num=50
flow_in = pn.pores('left')
flow_out = pn.pores('right')
max_seq = np.max([np.max(ip['pore.invasion_sequence']),
      np.max(ip['throat.invasion_sequence'])])
start = max_seq//Snwp_num
stop = max_seq
step = max_seq//Snwp_num
Snwparr = []
Swparr = [] #for Swp calc.
relperm_nwp = []
relperm_wp = []
```

In[23]:

```
#Calculating relative permeability continues
for i in range(start, stop, step):
    co2.regenerate_models();
    brine.regenerate_models();
    sat = sat_occ_update(network=pn, nwp=co2, wp=brine, ip=ip, i=i)
    Snwparr.append(sat)
    Swparr.append(1-sat) #for Swp calc.
    Rate_abs_nwp = Rate_calc(pn, co2, flow_in, flow_out, conductance = 'throat.hydraulic_conductance')
    Rate_abs_wp = Rate_calc(pn, brine, flow_in, flow_out, conductance = 'throat.hydraulic_conductance')
    Rate_enwp = Rate_calc(pn, co2, flow_in, flow_out, conductance = 'throat.conduit_hydraulic_conductance')
    Rate_ewp = Rate_calc(pn, brine, flow_in, flow_out, conductance = 'throat.conduit_hydraulic_conductance')
    relperm_nwp.append(Rate_enwp/Rate_abs_nwp)
    relperm_wp.append(Rate_ewp/Rate_abs_wp)
```

In[24]:

```
#Plotting the relative permeability curve
plt.figure(figsize=[8,8])
plt.plot(Swparr, relperm_nwp, '*-', label='Kr_nwp')
plt.plot(Swparr, relperm_wp, 'o-', label='Kr_wp')
plt.xlabel('Swp')
plt.ylabel('Kr')
plt.title('Relative Permeability in x direction')
plt.legend()
```

In[25]:

```
#Calculating the porosity of the network
Vol_void = np.sum(pn['pore.volume'])+np.sum(pn['throat.volume'])
inlet = pn.pores('left')
outlet = pn.pores('right')
A = op.topotools.get_domain_area(pn, inlets=inlet, outlets=outlet)
L = op.topotools.get_domain_length(pn, inlets=inlet, outlets=outlet)
Vol_bulk = A * L
Poro = Vol_void / Vol_bulk
print(f'The value of Porosity is: {Poro:.2f}')
```

B. Summary of Fluid Flow Modelling Approaches

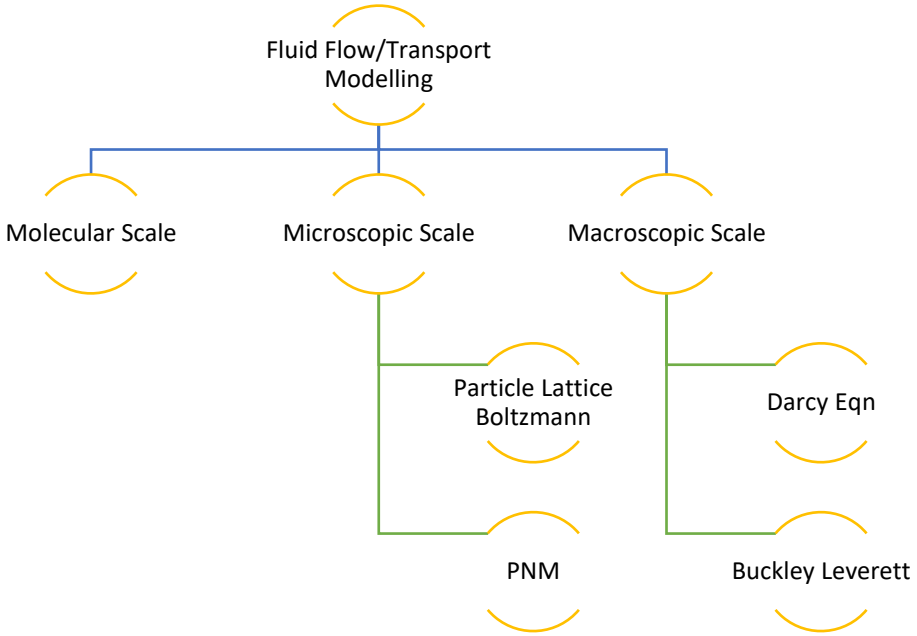

Figure 5.1 Chart summarizing fluid flow/ transportation models.

C. Summary of Network Design in PNM

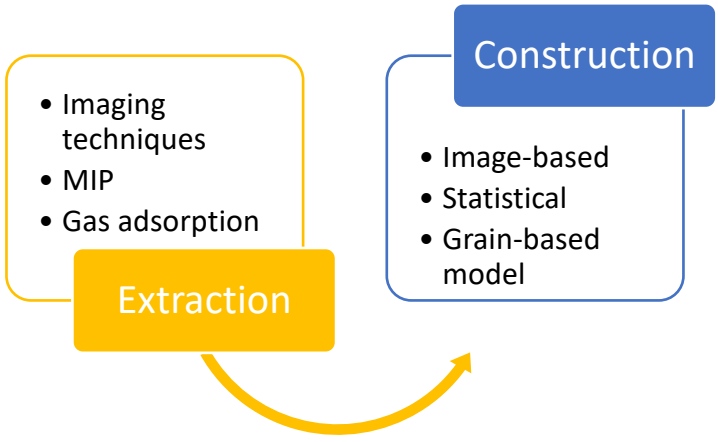

Figure 5.2 Summary of network construction techniques for PNM.

D. %Error Calculation

To calculate the %error, the individual deviations of the relative permeability values generated by OpenPNM from experimental values at selected saturations were calculated using the equation below. The average % error was then calculated from all the obtained error values.

$$\%Error = \frac{Actual\ value - Estimated\ Value}{Actual\ Value}$$

TEZ İZİN FORMU / THESIS PERMISSION FORM

PROGRAM / PROGRAM

Sürdürülebilir Çevre ve Enerji Sistemleri / Sustainable Environment and Energy Systems	*
Siyaset Bilimi ve Uluslararası İlişkiler / Political Science and International Relations	
İngilizce Öğretmenliği / English Language Teaching	
Elektrik Elektronik Mühendisliği / Electrical and Electronics Engineering	
Bilgisayar Mühendisliği / Computer Engineering	
Makina Mühendisliği / Mechanical Engineering	

YAZARIN / AUTHOR

Soyadı / Surname : Seif Hemed

Adı / Name : Thraiye

Programı / Program : Sustainable Environment and Energy Systems

TEZİN ADI / TITLE OF THE THESIS (**İngilizce** / English) : Determining CO_2-Brine Relative Permeability for CO_2 Sequestration: A Pore Network Modelling Study

TEZİN TÜRÜ / DEGREE**:** **Yüksek Lisans** / Master [*] **Doktora** / PhD [ ]

1. **Tezin tamamı dünya çapında erişime açılacaktır. /** Release the entire work immediately for access worldwide. [*]

2. Tez <u>iki yıl</u> süreyle erişime kapalı olacaktır. / Secure the entire work for patent and/or proprietary purposes for a period of **<u>two years</u>. *** [ ]

3. Tez <u>altı ay</u> süreyle erişime kapalı olacaktır. / Secure the entire work for period of **<u>six months</u>**. * [ ]

Yazarın imzası / Author Signature ..... **Tarih** / Date 31/08/2023

Tez Danışmanı / Thesis Advisor Full Name: Asst. Prof. Dr. Doruk Alp

Tez Danışmanı İmzası / Thesis Advisor Signature: ……..

Eş Danışmanı / Co-Advisor Full Name: N/A

Eş Danışmanı İmzası / Co-Advisor Signature: ……..

Program Koordinatörü / Program Coordinator Full Name: Asst. Prof. Dr. Canraş Batunlu

Program Koordinatörü İmzası / Program Coordinator Signature: ……..